UNIVERSIDADE FEDERAL DE SANTA CATARINA
PROGRAMA DE PÓS-GRADUAÇÃO EM ENGENHARIA
DE AUTOMAÇÃO E SISTEMAS

Felippe Schmoeller da Roza

A SMALL WIND GENERATION SYSTEM TO THE ON-BOARD CONTROL UNIT OF AN AWE SYSTEM

Florianópolis

2018

Felippe Schmoeller da Roza

A SMALL WIND GENERATION SYSTEM TO THE ON-BOARD CONTROL UNIT OF AN AWE SYSTEM

Dissertação submetida ao Programa de Pós-Graduação em Engenharia de Automação e Sistemas para a obtenção do Grau de Mestre em Engenharia de Automação e Sistemas.
Orientador: Prof. Alexandre Trofino Neto, Dr.
Coorientador: Prof. Ivo Barbi, Dr.

Florianópolis

2018

Ficha de identificação da obra elaborada pelo autor,
através do Programa de Geração Automática da Biblioteca Universitária da UFSC.

Roza, Felippe Schmoeller da
A small wind generation system to the on-board control unit of an awe system / Felippe Schmoeller da Roza ; orientador, Alexandre Trofino, coorientador, Ivo Barbi, 2018.
147 p.

Dissertação (mestrado) - Universidade Federal de Santa Catarina, Centro Tecnológico, Programa de Pós Graduação em Engenharia de Automação e Sistemas, Florianópolis, 2018.

Inclui referências.

1. Engenharia de Automação e Sistemas. 2. Turbina eólica. 3. AWE. 4. Rastreamento de potência. 5. Control pod. I. Trofino, Alexandre. II. Barbi, Ivo. III. Universidade Federal de Santa Catarina. Programa de Pós-Graduação em Engenharia de Automação e Sistemas. IV. Título.

Felippe Schmoeller da Roza

A SMALL WIND GENERATION SYSTEM TO THE ON-BOARD CONTROL UNIT OF AN AWE SYSTEM

Esta Dissertação foi julgada aprovada para a obtenção do Título de “Mestre em Engenharia de Automação e Sistemas”, e aprovada em sua forma final pelo Programa de Pós-Graduação em Engenharia de Automação e Sistemas.

Florianópolis, 11 de junho de 2018.

Prof. Werner Kraus Junior, Dr.
Coordenador do Programa de Pós-Graduação em Engenharia de Automação e Sistemas

Banca Examinadora:

Prof. Alexandre Trofino Neto, Dr.
Presidente - DAS UFSC

Prof. Carlos Illa Font, Dr.
UTFPR

Prof. Daniel Juan Pagano, Dr.
DAS UFSC

Prof. Marcelo de Lellis Costa de Oliveira, Dr.
DAS UFSC

ACKNOWLEDGEMENTS

I would first like to thank my advisors Alexandre Trofino and Ivo Barbi for steering me in the right direction whenever I needed it. Thank you very much, know that I appreciate all you have done for me.

I would also like to thank all support from the UFSCKite members, who are passionate to promote our group and AWE technologies, aiming for a brighter future where energy is available for everyone without prejudicing our planet. A special remark to Ramiro Saraiva, that gave valuable tips and was ever open to share his knowledge, and Helmut Araújo, who was always present during the experimental tests and able to help whenever it was necessary.

Finally, I must express my very profound gratitude to my wife Manoela, my parents Eliseu and Iva and my brother Matheus, for providing me with unfailing support and continuous encouragement throughout my years of study and through the process of researching and writing this thesis. This accomplishment would not have been possible without them. Thank you.

"All we have to decide is what to do with the time that is given us."
(J.R.R Tolkien, The Fellowship of the Ring)

"Wisdom is a shelter as money is a shelter, but the advantage of knowledge is this: Wisdom preserves those who have it."
(Ecclesiastes 7:12, NIV)

ABSTRACT

This master thesis deals with the design of a wind power system developed to provide energy to the control pod of a pumping kite system, one of the most popular AWE (Airborne Wind Energy) configurations so far. The control pod is the unit responsible for manipulating the airfoil steering tethers in order to control its flight. Having a system to charge the batteries embedded in the control pod is still one of the challenges that withstands against this technology to become a commercially viable product. Such charging system would allow to build a pumping kite prototype that can operate continuously and perform long term experiments to attest its robustness. This work presents the design of all elements used to build the developed wind turbine, beginning with the rotor, the element that converts the wind kinetic energy into mechanical energy, the generator, responsible for converting the mechanical energy into electric power, the rectifier and the DC-DC converter, respectively responsible to rectify the generator three-phase sinusoidal output voltage into DC voltage and control the rectified voltage, a battery storage system and the sensors needed to operate the system. Besides that, three maximum power point tracking (MPPT) methods are shown: optimal tip-speed ratio control (OTSR), power signal feedback (PSF) and perturb and observe (P&O). This work also deals with the design of further elements necessary to the experimental tests realization, such as an acquisition board used to measure the most important quantities and implement the converter control. To allow the realization of simulation tests a method that uses experimental data and the least squares algorithm to model the rotor is proposed. Methods to model the other system components are also discussed. OTSR and PSF MPPT methods were evaluated by using simulation models. Experiments with the built prototype were conducted in a wind tunnel and experimental results obtained with the P&O MPPT method are presented.

Keywords: Wind Turbine. AWE. Control pod. MPPT. DC-DC converter.

RESUMO

Essa dissertação de mestrado aborda o projeto de um sistema de geração eólica, desenvolvido para fornecer energia ao *control pod* de um sistema *pumping kite*, uma das configurações mais populares dentre os sistemas AWE (*Airborne Wind Energy*). O *control pod* é a unidade responsável pelo controle da trajetória do aerofólio por meio da manipulação dos seus cabos de comando. A ausência de um sistema para carregar as baterias do *control pod* é um dos desafios que impedem esta tecnologia de se tornar um produto comercialmente viável. Com este sistema a construção de um protótipo que permita uma operação contínua seria possível e testes a longo prazo que atestem a robustez do sistema poderiam ser realizados. O trabalho apresenta o projeto de todos os componentes que fazem parte da turbina eólica de pequeno porte desenvolvida, sendo estes o rotor, que é o elemento que realiza a transformação da energia cinética do vento em energia mecânica, o gerador, responsável por realizar a conversão da energia mecânica em potência elétrica, o retificador e conversor CC-CC, responsáveis respectivamente por retificar a tensão senoidal trifásica da saída do gerador e controlar a tensão retificada, um sistema de armazenamento por baterias e os sensores necessários para a operação do sistema. Além disso, três técnicas de rastreamento de potência (MPPT) são apresentadas: *optimal tip-speed ratio control* (OTSR), *power signal feedback* (PSF) e perturba e observa (P&O). O trabalho aborda também o projeto de outros elementos necessários para realização dos testes, como uma placa de aquisição de dados que é utilizada para medir as principais variáveis de interesse e implementar o controle do conversor. Para a realização de simulações, um método para modelagem do rotor utilizando dados experimentais e o algoritmo mínimos quadrados é proposto. A modelagem dos outros elementos do sistema também é discutida. Dois métodos de MPPT foram testados utilizando modelos de simulação, o OTSR e o PSF. Testes experimentais com o protótipo construído foram realizados em um túnel de vento e resultados experimentais obtidos com a implementação do método P&O são apresentados.

Palavras-chave: Turbina eólica. AWE. Control pod. MPPT. Conversor CC-CC.

LIST OF FIGURES

LIST OF TABLES

LIST OF ABBREVIATIONS AND ACRONYMS

AC	Alternating Current
ABS	Acrylonitrile Butadiene Styrene
AWE	Airborne Wind Energy
BLDC	Brushless DC
BJT	Bipolar Junction Transistors
CCCV	Constant Current Constant Voltage
DAQ	Data Acquisition
DC	Direct Current
EMF	Electromotive Force
FET	Field-Effect Transistors
HDPE	High Density Polyethylene
IC	Integrated Circuit
IGBT	Insulated-Gate Bipolar Transistor
LED	Light-Emitting Diode
MPP	Maximum Power Point
MPPT	Maximum Power Point Track
OTSR	Optimum Tip-Speed Ratio Control
PCB	Printed Circuit Board
PMSM	Permanent Magnet Synchronous Machines
P&O	Perturbation and Observation
PSF	Power Signal Feedback
SOC	State-Of-Charge
SOH	State-Of-Health

LIST OF SYMBOLS

$\dot{m}$	Mass flow rate
V_w	Wind speed
ρ	Air volumetric density
R_b	Rotor radius
C_p	Rotor power coefficient
P_m	Rotor mechanical power
λ	Tip speed ratio
ω_m	Rotor and generator rotational speed
β	Rotor blades pitch angle
K_w	BLDC machine back-EMF constant
T_e	BLDC machine electrical output torque
T_l	BLDC machine load torque
V_m	Three-phase diode bridge input voltage peak
D	Duty cycle
V_{Dmax}	Diode bridge maximum diodes reverse voltage
η	Wind turbine electrical efficiency
P_E	Wind turbine electrical output power
E_0	Battery constant voltage
K	Battery polarization voltage
Q	Battery capacity
A	Battery exponential zone amplitude
B	Battery exponential zone time constant inverse
f_s	DC-DC converter switching frequency

CONTENTS

1 INTRODUCTION

Energy plays such an important factor in our lives that nowadays is hard to think in reaching quality of life without a proper provision of energy. In fact, energy is essential to support economic and social progress since the beginning of the human society. As an example, the ability to control and create fire led to a deep change in the habits of early humans. The changes vary from the diet to behavior, geographical dispersion, expansion of the activities into the dark and colder hours of the day, among many others. Since then several innovations happened, associated to new ways to transform and store energy from different sources. Coal was burned for heating and cooking purposes in China more than 3000 years ago. Ancient Greeks used to build water wheels in rivers to irrigate the crop. Persians built windmills to pump water and grind grains around the year 500 AD. Water and steam powered engines were major pieces in the industrial revolution.

But it was the advances in the studies of electromagnetism, driven by brilliant minds as André-Marie Ampère, Michael Faraday and James Clerk Maxwell, that made life in society change drastically in less than 200 years. Now energy is not only a source of heat and light, as fire was to prehistoric man, neither is something only used by the factories or transportation vehicles, as steam powered engines during XVIII century, today energy is something human society depends 24 hours a day. According to the International Energy Agency, with the growing industrialization, the demand for energy will just continue to grow for many years. Figure 1 shows the estimated increase on energy demand by region, in million tonnes of oil equivalent, from 1990 to 2040.

Providing energy using coal and petrol was a standard until the energy crisis of the 1970s, but then it became clear that depending so much on non-renewable sources of energy, available in such a few places, would lead to an occasional collapse in the future. To avoid this scenario, most of the highest energy consumption countries started to look for ways to harvest energy from alternative sources, allowing to attend this increasing demand of energy. Today renewable energy sites are spreading fast around the world, driven mostly by solar and wind power stations, although coal and oil are still the global primary energy sources as showed in Figure 2.

In order to increase the renewable energy share in the global mix and to make energy available and cheap in long term, scientists

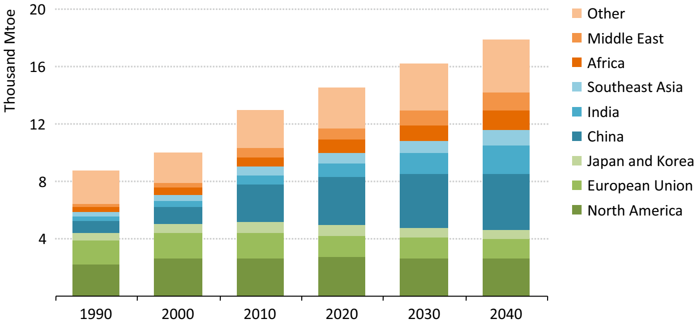

Figure 1 – Energy demand by region. Source: (IEA, 2016).

and researchers are looking for new ways to harvest energy. The ideal is to produce energy minimizing both costs and environmental impacts. Solar panels and wind turbines are already being used in a commercial scale, with the former representing the fastest growing source of energy. In order to turn into a commercially viable alternative, wind turbines have been developed to produce more power, as shown in Figure 3. The increase in the turbine sizes is noticeable due to the fact that available power is a function of the area. Also, stronger and steadier winds are present in higher altitudes. However physical and economical constraints are related to conventional wind power systems since increasing the size of wind turbines leads to many technical difficulties (PRAMOD et al., 2017).

In order to keep innovation in wind generation and to increase its potential, many institutions and business companies are researching an alternative design concept known as Airborne Wind Energy (AWE). AWE aims in developing wind power systems without the structural elements that are present in conventional wind turbines. Therefore, reaching and exploring winds in higher altitude becomes cheaper and more competitive when compared to non-renewable sources.

1.1 AIRBORNE WIND ENERGY

AWE technologies focus in dismissing the need of massive wind turbine structures by using light and flexible tethers, allowing the sys-

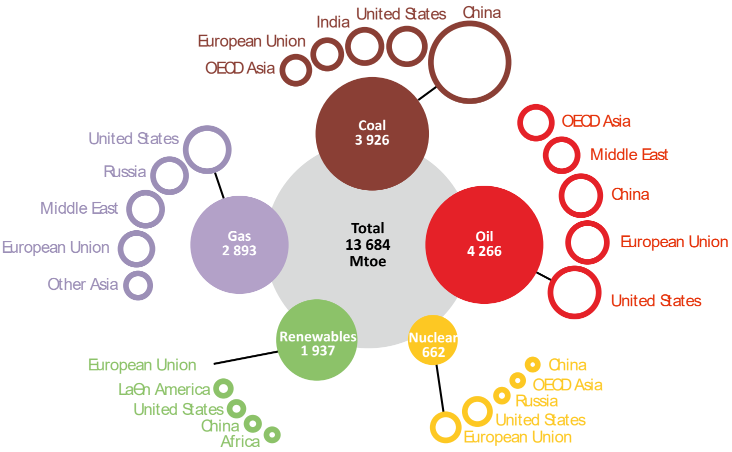

Figure 2 – Global primary energy mix in 2014, in Million Tonnes of Oil Equivalent. Source: (IEA, 2016).

tem to operate above 200m from the ground, taking advantage of the faster and more consistent wind available in such altitudes, with relatively low capital costs.

Intuitively, one first approach to generate power from the wind without a tower is to use a flying tethered airplane, or a kite, carrying a wind turbine and flying in a trajectory approximately perpendicular to the wind relative to the ground - the so-called crosswind operation. The power generation occurs due to the plane's high relative airspeed. This method is called on-board generation or *drag mode* system, because the airplane has a increased drag due to the turbine. This type of system is relatively simple, however escalating the power production is not an easy task because of the difficulties in designing a plane that can carry a big generator. Also, security measures must be implemented because carrying such heavy load is somehow risky.

Alternatively, the electric generator can be placed on the ground, connected to the airplane by a tether. This is called ground-based generation or *lift mode* system. In this type of system a drum is attached to the generator's shaft and the lift power of the airplane is used to roll and unroll the tether from the drum. This rotation over the shaft is responsible for the power generation. To allow the continuous operation of a lift mode system it is necessary to retract the tether eventually.

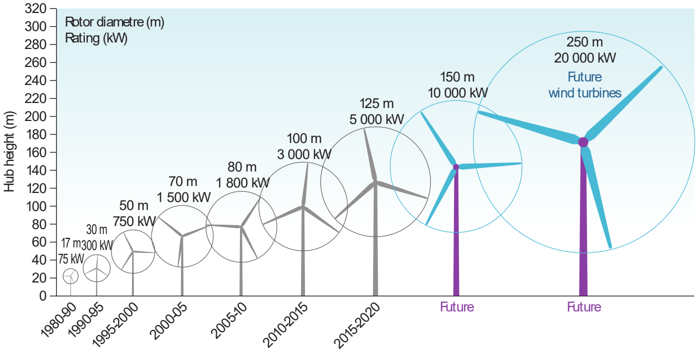

Figure 3 – Growth in size and rated power of wind turbines since 1980 and prospects. Source: (IEA, 2013).

To spend less power retracting the tether then what was generated, it is necessary to use a flight pattern that produces the minimum lifting force as possible, leading to a positive balance in the power production. Due to its periodically changing behavior, lift mode is also called *pumping mode* or *yo-yo mode*. Figure 4 shows the operation of both drag and lift modes compared to a conventional wind turbine.

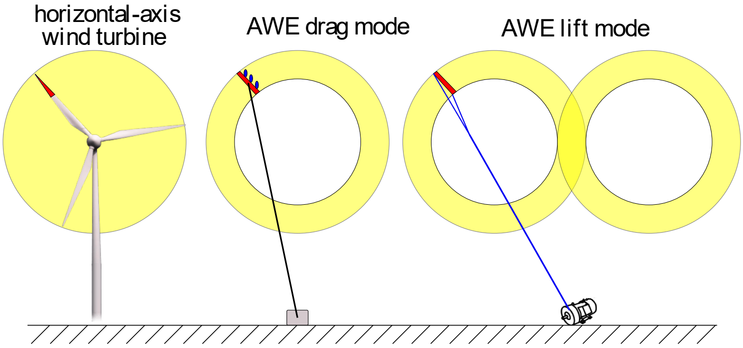

Figure 4 – AWE drag and lift modes. Source: (De LELLIS, 2016).

AWE technology represents a revolution in harvesting energy from the wind, however such systems are way more complex to develop and operate when compared to the already established conventional wind turbines. Several companies and academic research groups worldwide are developing and researching AWE prototypes, but system reliability and robustness during power generation has not been demonstrated yet, at least by the publicly available literature.

Operating an AWE system involves the interaction of ground-based equipments with long and flexible tethers with the aircraft immersed in an uncertain and variable wind field. Differently from wind turbines, that are turned off when the wind surpasses extreme conditions, AWE systems must have some procedure to autonomously takeoff and land. Developing such a method, viable technically and economically, is prerequisite for a long-term experimental AWE system validation (FAGIANO et al., 2018).

Several institutions worldwide are conducting development and research activities in AWE technologies, as shown in Figure 5. This work was developed inside the UFSCKite group, that carries out research in AWE systems focusing in the pumping kite model, located in the Federal University of Santa Catarina - Brazil.

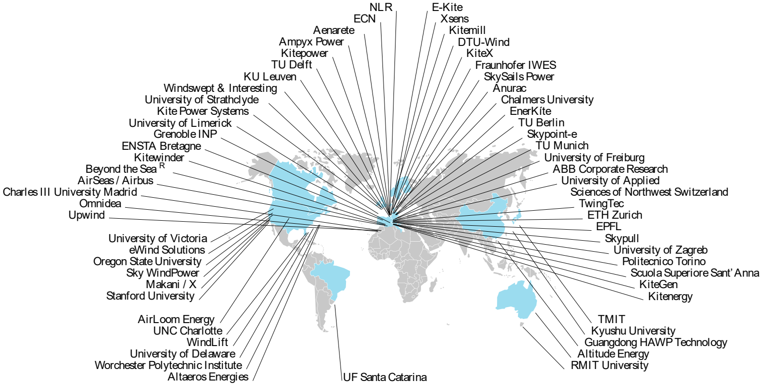

Figure 5 – AWE research and development groups worldwide. Source: (AHRENS; DIEHL; SCHMEHL, 2017).

1.1.1 Pumping kite

Pumping kite is basically a lift mode AWE system implemented with a single or multiple kites and it is one of the most popular configurations in the AWE literature so far. One of the reasons is that it allows to build a prototype using kitesurfing and paragliding kites, available in the market with relatively low cost. The flexible kite can also be replaced by a rigid wing, that has a higher aerodynamic efficiency and simplifies the launching and landing operation in some aspects (De LELLIS, 2016).

As aforementioned, a pumping mode operation consists in two distinct phases. In the traction phase - also called active phase - the tether is reeled out from the drum and the ground station machine works as a generator. During this phase the kite follows a trajectory of a lemniscate (∞), allowing the system to fly continuously without twisting the main tether. The retraction phase - or passive phase - starts when a preset tether length is reached. It consists in reeling the tether back around the drum, with the machine working as a motor. Figure 6 exemplifies the trajectory performed by a pumping kite system during its operation.

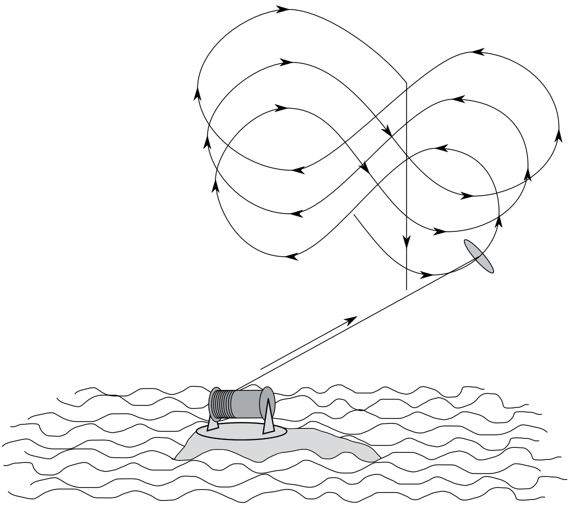

Figure 6 – Pumping kite trajectory example. Source: (ARGATOV; RAUTAKORPI; SILVENNOINEN, 2009).

A pumping kite system consists, mainly, of a kite, a control unit - responsible to control the flight trajectory of the kite - usually called *control pod* and the ground station, where the electric generator is located. Figure 7 shows a more detailed overview about the components of a pumping kite system and how they are connected.

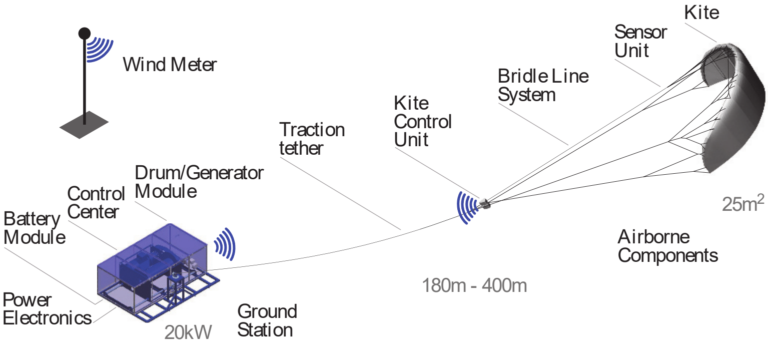

Figure 7 – Pumping kite system components. Source: (VLUGT; PESCHEL; SCHMEHL, 2013).

1.1.2 Control Pod

In order to control the kite's flight trajectory a control unit, called control pod, with the actuators needed to manipulate the steering tethers is necessary. It is the airborne steering unit responsible for the automatic control of the kite under several operating conditions. Besides the manipulators, many other elements can be embedded inside the control pod, such as sensors, controllers, a battery and optionally, wireless communication system components and additional safety systems.

The control pod controls the kite by pulling in one tether and releasing the other. This creates a difference in left and right tether lengths, deforming the kite's profile and tilting the lift vector to one side, thereby resulting in a change in its direction.

Figure 8 shows the control pod design for the first UFSCkite research group prototype. This control pod, particularly, was designed to stay on the ground, as a proof of concept for the kite trajectory control. In order to fly along with the kite at high altitudes, a new design should be done taking into account the aerodynamics and total weight, parameters that impact directly the efficiency of a pumping kite system.

A recurring problem is that to allow a pumping kite system to work continuously, the control pod must have some source of energy, otherwise the flight will be limited to its battery autonomy. An op-

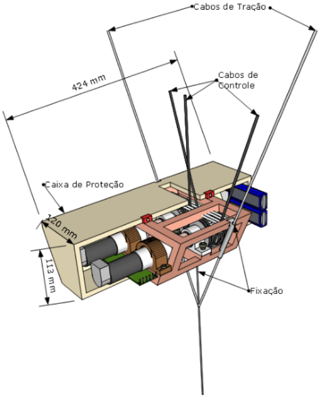

Figure 8 – Control pod design of UFSCKite research group's first prototype.

tion is to supply the electrical power from the ground, through cables embedded within the kite's traction tether. However, this limits the tether length due to the increasing weight and drag added by such cables (PAULIG; BUNGART; SPECHT, 2013). An additional drawback is that achieving the desired tether mechanical properties is extremely difficult if it is necessary to insert an electrical cable within it.

1.2 OBJECTIVES

Providing a control pod with a time-unlimited energy supply is still a barrier for developing a pumping kite AWE system that can work continuously. As aforementioned, the altitude of operation turns the possibility of providing a power cable from the ground into an unfeasible alternative. The solution is to embed an energy generation system in the control pod.

The first option would be to attach a solar panel to the control pod. However, it would add too much weight to the system. For example, an AMERESCO SOLAR© 60 W solar panel weights 6 kg (AMERESCO SOLAR, 2015). Even removing the aluminum frame and the protecting glass in order to reduce its weight, this kind of panel requires a large area to produce energy- this same 60 W panel has an area of 0.45 m^2. Besides that, solar energy is not always available, making it impossible to grant a continuous operation for the AWE system unless a high capacity battery is used to provide energy during the night and cloudy days.

This work proposes the development of a wind turbine system, small enough to be attached to the control pod without affecting the AWE system operation significantly. To the best of my knowledge, (KIEBOOM, 2017) is the only similar work available in the literature. His approach differ greatly from what this thesis proposes, focusing in the rotor design and manufacturing along with a rich and relevant study about the noise that such system can produce during its operation. This work, however, is focused in the development of the wind turbine system itself, that will be embedded into the control pod. The blade design and all mathematical background needed to manufacture a rotor is well described in the aforementioned thesis. Instead, this work uses commercial blades to manufacture the rotor. Furthermore, the design of each further element in addition to methods intended to optimize the generated power will be presented.

Using the models provided by (SILVA et al., 2014) it is possible to compute the wind velocity available for the generation system. Figure 9 shows results from a simulation of a pumping kite system with an $17\,\mathrm{m}^2$ airfoil, flying at an altitude range that varies from $270\,\mathrm{m}$ to $500\,\mathrm{m}$. This pumping kite prototype, developed by UFSCKite research group, is designed to produce a nominal power of $12\,\mathrm{kW}$. The figure displays the apparent wind that faces the control pod, the airfoil speed and the traction tether length.

Analyzing Figure 9, the cyclic behavior of the system becomes evident. In the first cycle the airfoil speed follows a sinusoidal pattern, related to the spiral trajectory of the kite during the traction phase, while the tether is reeled out from the drum and its length increases. Then the tether is reeled back and the airfoil speed moves slower in a flat pattern. It is important to notice that during the whole kite trajectory, the apparent wind presents a significant value, allowing to charge the batteries throughout the entire operation. During both phases, the apparent wind varies from approximately $20\,\mathrm{m\,s^{-1}}$ to $30\,\mathrm{m\,s^{-1}}$, something between $70\,\mathrm{km\,h^{-1}}$ and $110\,\mathrm{km\,h^{-1}}$.

It is estimated that an AWE pumping kite system with such characteristics would demand an average power of $60\,\mathrm{W}$ from the control pod, hence the on-board generation system must be designed to supply this power for every expected apparent wind speed. Also, the system must supply a voltage near to $24\,\mathrm{V}$, in order to attend the actuators requirements. To maintain the voltage as steady as possible, a battery with the proper attributes must be designed. The main objectives of

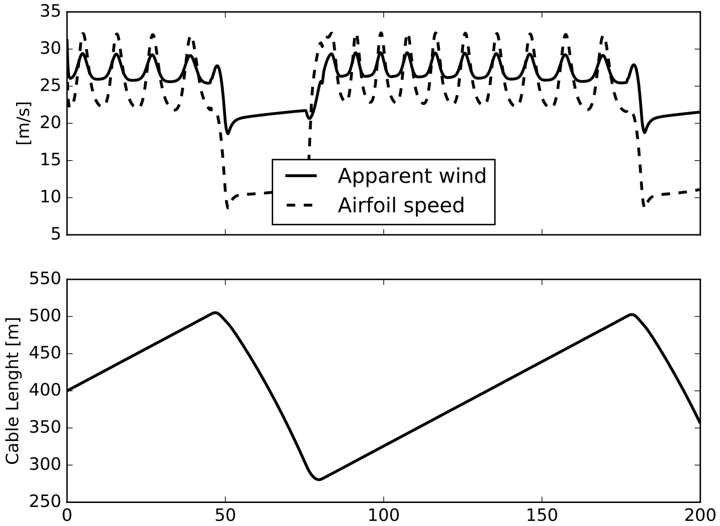

Figure 9 – Apparent wind, airfoil speed and cable length in pumping kite system simulation.

this work can be summarized as:

- To design a micro wind turbine that works with wind speeds in a range from $20\,\mathrm{m\,s^{-1}}$ to $30\,\mathrm{m\,s^{-1}}$ and is capable to generate 60 W of average power.
- The system must be embedded into an AWE pumping kite control pod, then reducing its dimensions and weight is necessary.
- To design a 24 V battery pack that fulfills the electrical, mechanical and safety requirements related to this system;
- To develop a DC-DC converter able to control the turbine output rectified voltage, allowing the power tracking.
- To develop models for the system allowing to perform simulations and evaluate its performance before any experimental tests.
- To implement proper MPPT methods to optimize the generation for the available wind power, although the system is not intended

> to work continuously in the maximum power point, that adds extra drag and can prejudice the AWE system throughout critical moments, as while the landing and takeoff operation and during some segments of the AWE lemniscate trajectory, where the system speed is low.

The work is organized as follows. In Chapter 2 the fundamentals needed to design the desired wind power system are presented. Firstly, understanding the properties of the wind is indispensable to model and work with a wind powered system. Next, in order to understand how a small-scale wind turbine works, the system is separated into several subsystems: the rotor, the generator, the rectifier, the DC-DC converter, the battery and the sensors. In addition, some MPPT techniques are explored, essential to exploit the most of available wind power.

Chapter 3 deals with the design of each module of the proposed system. It begins with the mechanical design of a new *control pod*, necessary to embed the wind power system. Then it is shown how to choose and model the rotor for achieving the desired requirements. The chapter continues with the design of the battery pack, that consists in choosing the better technology that fulfills the electrical and security requirements. The design of the proposed DC-DC converter is then presented.

Chapter 4 is concerned with some techniques to model the designed components. Modeling the system is necessary to evaluate the performance with proper simulations before performing experiments.

In Chapter 5, some simulations with the modules previously modeled are presented, beginning with the DC-DC converter results. Then some simulation results with the battery model show how the manufacturer proposed charging method works, increasing the state of charge and also its output voltage. Then some open-loop simulations with the entire system are presented. The last results concern to simulations of the MPPT methods with the turbine model.

The focus of Chapter 6 is to present the experimental results. It begins with tests with the developed DC-DC converter to attest if the results are according to the design specifications. Then the proposed MPPT method is implemented and tested with the wind turbine in a wind tunnel.

Lastly, the concluding remarks are disposed in Chapter 7.

2 WIND POWER SYSTEMS

This chapter is an overview of the construction of a wind turbine, how it works and the elements that are present in such systems. Although the focus is on small-scale wind turbine systems, some elements and techniques usually related to large turbine systems will be also mentioned.

A wind power system is basically composed by a rotor, a generator and the tower foundation. Additional components may be present, as a gearbox, a break system - either electrical or mechanical -, an yaw motor and driver, an anemometer, a tachometer or encoder, converters and inverters, among others. Figure 10 illustrates the components that may be present in a wind turbine system.

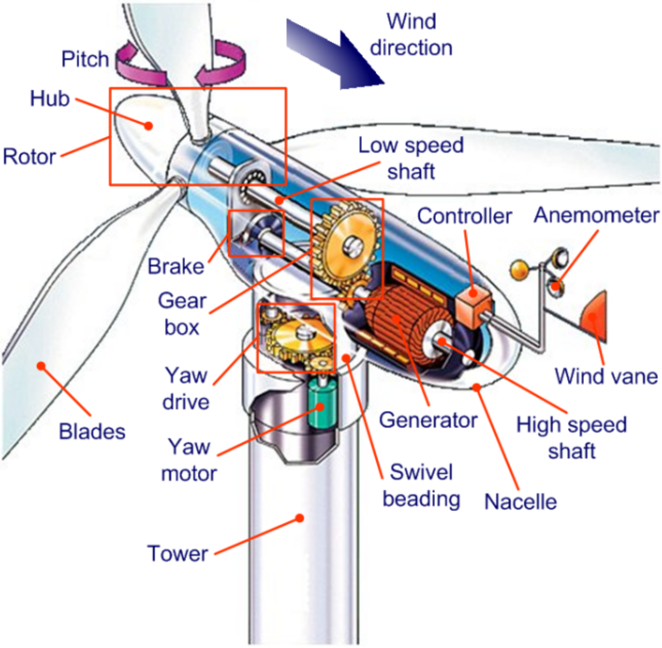

Figure 10 – Components of a wind power system. Source (MAHMOUD; XIA, 2012).

In small-scale systems, however, some of those elements are not usual whereas other are more frequent, as storage batteries. If the system works with an alternating current generator, it is necessary to use a rectifier to connect the battery to the system. A DC-DC converter is an element that allows to control the speed of rotation through stall control. A battery management system (BMS) may also be present. Moreover, most of the small-scale turbines present fixed pitch blades.

A small-scale wind power system diagram is shown in Figure 11.

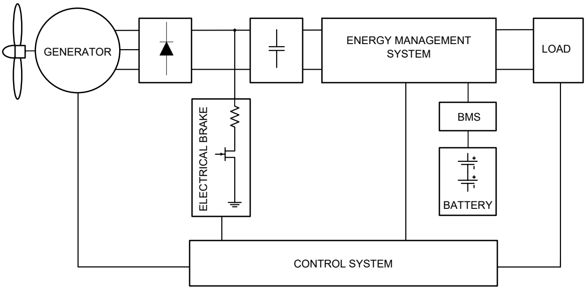

Figure 11 – Diagram of a small-scale wind power system.

2.1 WIND AVAILABLE ENERGY

For modeling and designing the elements of a wind turbine system, it is important to quantify the energy available in the wind and how much of this energy can be converted into mechanical power by the turbine rotor.

The mass flow rate equation for a fluid is given by the following surface integral:

$$\dot{m} = \int\int_A \rho V_w \cdot dA \tag{2.1}$$

where ρ is the mass density of the fluid, A is the cross-section area and V_w is the wind velocity.

For a plane area, as a cylinder section, the equation can be written as:

$$\dot{m} = \rho A V_w \tag{2.2}$$

The kinematic energy of a mass m with the velocity v is:

$$E = \frac{1}{2} m V_w^2 \tag{2.3}$$

And the energy rate for the nominal fixed velocity, which is the power P, will be:

$$P = \dot{E} = \frac{1}{2}\dot{m}V_w^2 \tag{2.4}$$

From Equation (2.2) and Equation (2.4) we obtain the Equation that describes the available wind power in a cross-section area:

$$P = \frac{1}{2}\left(\rho A V_w\right) V_w^2 = \frac{1}{2}\rho A V_w^3 \tag{2.5}$$

For a horizontal axis wind turbine the cross-section area is a cylinder, then the equation can be written as:

$$P = \frac{1}{2}\rho \pi r^2 V_w^3, \tag{2.6}$$

where r is the rotor radius.

A coefficient that express the efficiency of a rotor in converting wind power into mechanical power may be used to obtain the output power for a given wind speed. This coefficient, called *power coefficient* - C_p, can be expressed as:

$$C_p = \frac{Power\ extracted}{Power\ available\ in\ the\ Wind} \tag{2.7}$$

The theoretical maximum C_p value of an ideal wind turbine rotor, known as the Betz limit, is 16/27 (KUIK, 2007).

The rotor mechanical output power, P_m, is represented by the following equation:

$$P_m = \frac{1}{2}\rho A V_w^3 C_p \tag{2.8}$$

2.2 ROTOR

The rotor is a mechanical device that turns round propelled by lift or drag forces from the interaction with the wind, responsible to convert the wind energy into rotational kinetic energy. A wind turbine can be classified as a vertical-axis or horizontal-axis depending in how the rotor is positioned. Figure 12 shows a design example for both technologies.

Only horizontal-axis turbines will be treated in this work. It is the predominant design in the literature and among commercial wind turbines. It is composed of a group of blades mounted into a central

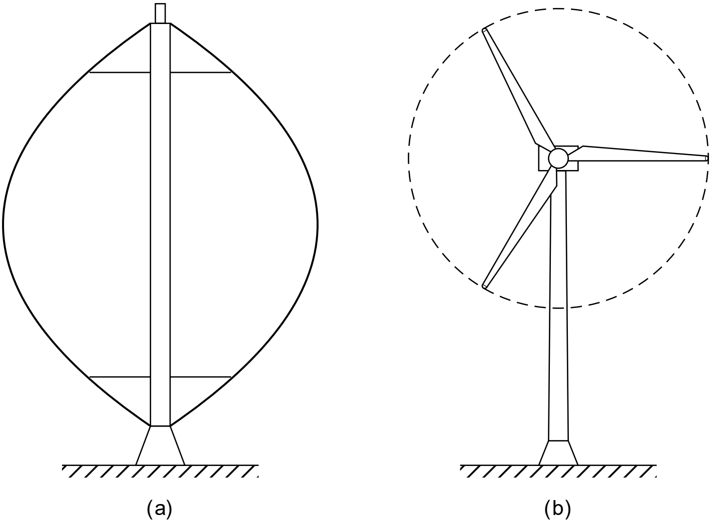

Figure 12 – (a) Vertical-axis and (b) horizontal-axis wind turbines. Source: (BIANCHI; MANTZ; BATTISTA, 2007).

hub, that is connected to the turbine main shaft.

The mechanical power a rotor can extract from the wind depends on several factors: the blade length, the blade pitch, its geometry, the wind velocity, the air density, etc.

The simplest rotor type is the fixed-pitch rotor, present in stall-regulated wind turbines. Since the power output depends on the pitch, this rotor is designed based on the expected average wind velocity. On the other hand, a pitch-regulated turbine allows changing dynamically the pitch of the blades. Controlling the blade pitch allows to extract the maximum power when wind velocity changes. It is also used during the turbine start up, when the rotational speed is low, helping the turbine to speed to the nominal rotation faster (JAIN, 2011).

Stall-regulated rotors are simpler and less expensive because the mechanisms to change the pitch of the blades increase the rotor design complexity significantly. Besides that, motors and further elements are necessary to control the pitch. Pitch-regulated rotors are more common in large systems where every increase in the system efficiency represents a noticeable return of the monetary investment.

2.2.1 Rotor model

Having a model for the rotor is important to understand the behavior of the system under several conditions. Basically, the rotor model is an equation that describes the power coefficient, C_p. Usually the power coefficient is modeled as a nonlinear function of the blade pitch angle, β, and the tip-speed ratio, λ. Tip-speed ratio is the relation between the wind speed, the angular speed and the rotor radius, as shown in Equation (2.9).

$$\lambda = \frac{\omega_m \cdot R_b}{v_w}, \tag{2.9}$$

where ω_m is the rotor rotational speed (in rad/ sec) and R_b is the rotor radius (in m). The rotor radius and its swept area are represented in Figure 13.

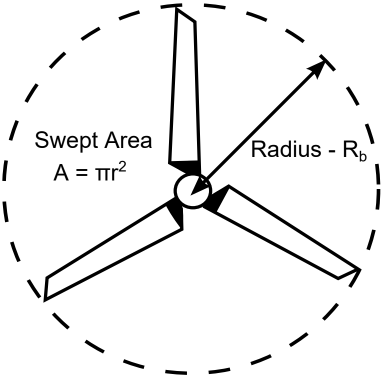

Figure 13 – Rotor swept area.

Several authors, such as (HEIER, 2014), (PETKOVIĆ; ĆOJBAŠIČ; NIKOLIĆ, 2013) and (KUMAR; CHATTERJEE, 2016), use the model given by Equation (2.10) to model the power coefficient as a function of the tip-speed ratio and the blades pitch angle.

$$C_p = k_1 \left(k_2\lambda_i - k_3\beta - k_4\beta^{k_5} - k_6\right) exp^{-k_7\lambda_i} \tag{2.10}$$

$$\frac{1}{\lambda_i} = \frac{1}{\lambda + 0.08\beta} - \frac{0.035}{1+\beta^3}, \tag{2.11}$$

where the turbine coefficients $k_1 - k_7$ must be fitted for the desired turbine. The coefficients are usually given by the manufacturer. Table 1 shows the coefficients used by (MANYONGE et al., 2012) to model a small wind turbine.

Table 1 – Turbine coefficients.

Coefficient	Value
k_1	0.5
k_2	116
k_3	0.4
k_4	0
k_5	1.5
k_6	5
k_7	21

Source: (MANYONGE et al., 2012).

Figure 14 shows the C_p as a function of the tip-speed ratio, λ, for a system with the coefficients from Table 1 and the rotor blade pitch angle fixed in 8°.

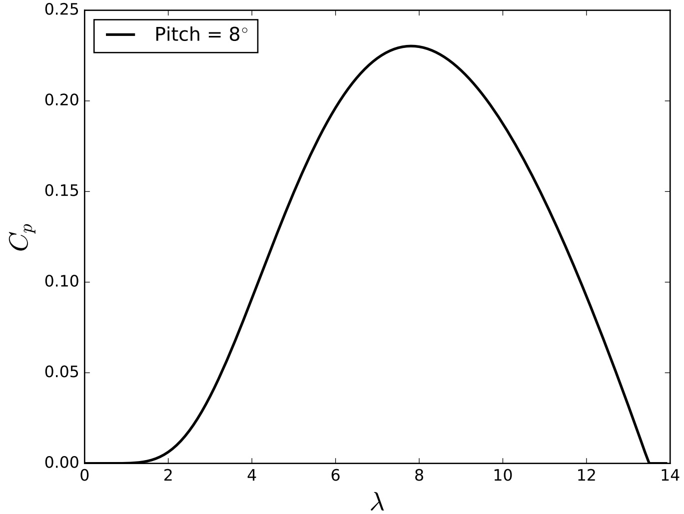

Figure 14 – Small wind turbine C_p model.

A different approach to model the turbine rotor was proposed by (WASYNCZUK; MAN; SULLIVAN, 1981). It consists in replacing the function to model the rotor for Equation (2.12), a simpler function that can also model a turbine if the parameters $C_1 ... C_4$ are chosen correctly. It is much easier to determine the values for the 4 coefficients from Equation (2.12) than adjusting the 8 coefficients from Equation (2.10). However, a function with fewer coefficients cannot represent some system characteristics that the more complex model sometimes is able to. To fit the model it is necessary to acquire experimental data, usually from a wind tunnel test, and use the least squares algorithm to fit the parameters. This alternative is recommended if the rotor model is not available or the model does not match the experimental results. The least squares algorithm is presented in Appendix C.

$$C_p = C_1(\lambda + C_2\beta^2 + C_3)e^{C_4\lambda} \tag{2.12}$$

With the C_p function properly fitted, it is possible to compute the output mechanical power of the rotor by using Equation (2.8).

2.3 GENERATOR

The electricity generator is a vital piece in a wind power system, being responsible to convert the mechanical power in the main shaft into electrical power. Basically the generator is a rotating electrical machine, composed by a stator - its stationary part, and the rotor - its moving part.

Usually the following technologies are used for small scale wind energy conversion systems: induction machines, brushless DC (BLDC) machines and permanent magnet synchronous machines (PMSM). BLDC and PMSM are similar machines, differing only in the stator construction - distributed stator windings in PMSM and salient field coils in BLDC - and the back electromotive force (EMF) wave form - sinusoidal in PMSM and trapezoidal in BLDC.

Although all devices have their pros and cons, BLDC is usually chosen for being a less expensive solution for small scale wind turbines (MILIVOJEVIC et al., 2008). Besides that, a BLDC machine operating as a generator offers further advantages. It can be controlled over a wide speed range with a high efficiency. BLDC are also known for having a good durability, high power density and presenting low maintenance. Also, when connected to a diode rectifier, the rectified DC output voltage has reduced pulsations, due to the trapezoidal phase shaped voltage

(LACZKO et al., 2015).

A BLDC machine is a type of synchronous motor, then the magnetic field in the stator and in the rotor rotates at the same frequency, not slipping as in an induction machine. There are single-phase, two-phase and three-phase BLDC machines, with the last being the most popular. Figures 15(a) and 15(b) shows, respectively, the diagrams of a single-phase and a three-phase BLDC machine.

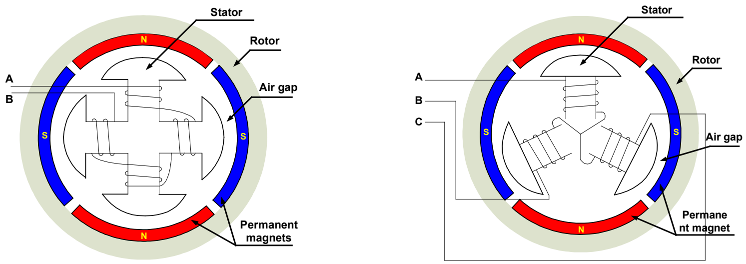

(a) Single-phase.

(b) Three-phase.

Figure 15 – BLDC machine diagrams.
Source: (ZHAO; YU, 2011).

The construction of a BLDC machine stator is similar to an induction machine, with stacked steel laminations to carry the windings. These windings are placed in slots which are axially cut along the inner periphery of the stator, arranged in either star or delta shapes with the first being the most usual. Each winding is constructed with many interconnected coils, with one or more coils being placed in each slot. In order to form an even number of poles, the windings are distributed over the stator periphery.

The rotor of a BLDC machine is made of permanent magnet, usually ferrite magnet for being a less expensive material. However, rare earth alloy magnets are gaining popularity due to its high magnetic density, allowing to produce a smaller rotor for the same desired torque (YEDAMALE, 2003). Constructively the magnets number can vary from two to eight alternate pole pairs (north and south), arranged in different ways, as showed in Figures 16(a) to 16(c).

It is common that BLDC machines have hall sensors embedded into the rotor. Hall sensors are important to BLDC machines operating as a motor, providing the information to synchronize the stator

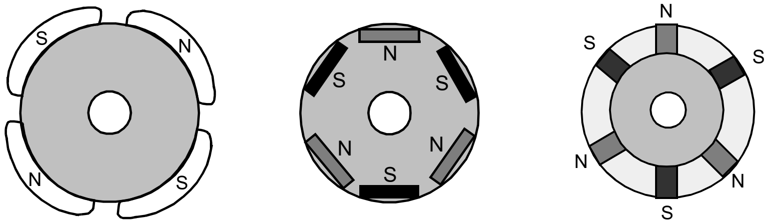

(a) Circular core with magnets on the periphery.

(b) Circular core with rectangular magnets embedded in the rotor.

(c) Circular core with rectangular magnets inserted into the rotor core.

Figure 16 – Rotor magnet cross sections.
Source: (YEDAMALE, 2003).

armature excitation with the rotor position. When the BLDC operates as a generator, this synchronization is not necessary, but the sensors can be used to determine the machine rotational speed.

2.3.1 Modeling

A BLDC machine can be modeled as a synchronous machine, differing only in some dynamical characteristics due to the permanent magnet being mounted on the rotor (TIBOR; FEDÁK; DUROVSKY, 2011). Equations (2.13) to (2.15) express the armature winding model for a three-phase BLDC machine.

$$V_a = Ri_a + L\frac{di_a}{dt} + e_a \tag{2.13}$$

$$V_b = Ri_b + L\frac{di_b}{dt} + e_b \tag{2.14}$$

$$V_c = Ri_c + L\frac{di_c}{dt} + e_c, \tag{2.15}$$

where L is the armature self-inductance [H]; R the armature resistance [Ω]; V_a, V_b and V_c the terminal phase voltages [V]; i_a, i_b and i_c the phase currents [A] and e_a, e_b and e_c the machine back-EMF [V].

The back-EMF wave form for each phase is modeled as a function of rotor position and proportional to its rotational speed. The equations are expressed by Equations (2.16) to (2.18).

$$e_a = K_w f(\theta_e)\omega_m \tag{2.16}$$

$$e_b = K_w f\left(\theta_e - \frac{2\pi}{3}\right)\omega_m \tag{2.17}$$

$$e_c = K_w f\left(\theta_e + \frac{2\pi}{3}\right)\omega_m, \tag{2.18}$$

where K_w is back-EMF constant of one phase [$\mathrm{V\,rad^{-1}\,s^{-1}}$], θ_e is the electrical rotor angle [° el.] and ω_m is the rotor speed [$\mathrm{rad\,s^{-1}}$]. The electrical rotor angle is given by Equation (2.19).

$$\theta_e = \frac{p}{2}\theta_m, \tag{2.19}$$

where p is the equal number of pole pairs and θ_m the mechanical rotor angle.

The electrical torque for each phase may be computed as the power divided by the rotor speed. The output torque is given by the sum of all torques, as shown in Equation (2.20).

$$T_e = \frac{e_a i_a + e_b i_b + e_c i_c}{\omega_m}, \tag{2.20}$$

where T_e is the total torque output [N m].

Equation (2.21) represents the mechanical model for a BLDC generator.

$$T_e - T_l = J\frac{d\omega_m}{dt} - B\omega, \tag{2.21}$$

where T_l is the load torque [N m], J the rotor inertia [$\mathrm{kg\,m^2}$] and B the friction constant [$\mathrm{N\,m\,s\,rad^{-1}}$].

2.4 RECTIFIER

A rectifier is an electronic circuit able to convert bidirectional voltage into unidirectional. It is an important element in power systems where the generator is an alternating current (AC) device and direct current (DC) is expected in the output.

Although it is possible to design a rectifier based in mechanical commutators, nowadays most of the circuits use semiconductor devices for being more reliable and efficient and allowing a much greater switching frequency(GRIGSBY et al., 2001). A semiconductor-based rectifier can also be called static rectifier.

Several static rectifier topologies have been developed, classified into two groups, the uncontrolled rectifiers and the controlled rectifiers.

2.4.1 Uncontrolled Rectifiers

The fundamental element of uncontrolled rectifiers is the diode, a semiconductor devices that ideally conducts current in only one direction. There are two types of uncontrolled rectification circuits, the half-wave rectifier and the full-wave rectifier. Half-wave rectifier requires a single diode in a single-phase supply and three diodes in a three-phase supply. Figures 17(a) and 17(b) show respectively the half-wave and full-wave circuits for a single-phase input. The three-phase rectifier circuits are shown in Figures 18(a) and 18(b).

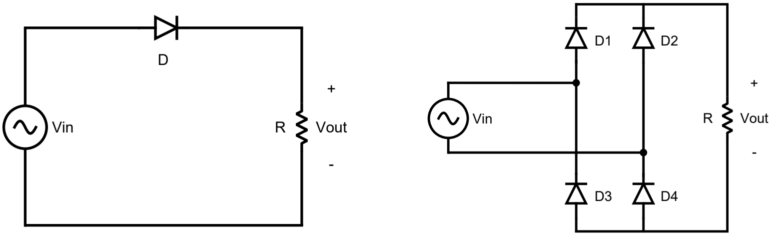

(a) Half-wave rectifier.

(b) Full-wave rectifier.

Figure 17 – Single-phase uncontrolled rectifiers.

Half-wave rectifiers let only half of the input voltage per phase to pass, leading to a larger voltage ripple across the load. In other hand, a full-wave rectifier is able to invert the negative voltages, taking advantage of the whole input voltage. Figure 19 shows the output of both half and full-wave rectifiers to a sinusoidal voltage input.

In order to smooth the output voltage and current an electronic filter can be applied. A passive filter consists of a capacitor, a choke or an arrange of capacitors, chokes and resistors. Usually full-wave rectifiers require a smaller filter capacitor as it will be charged twice as often than in a half-wave rectifier, being a most common choice for typical power supply projects. Nevertheless, it is important to notice that generally the full-wave rectifier will have a bigger loss associated to voltage drops across the diodes, as it requires more diodes. A full-wave

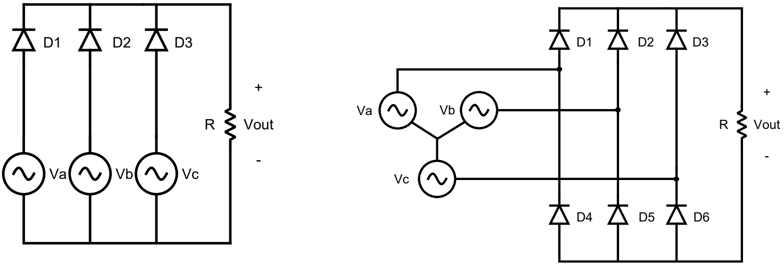

(a) Half-wave rectifier.

(b) Full-wave rectifier.

Figure 18 – Three-phase uncontrolled rectifiers.

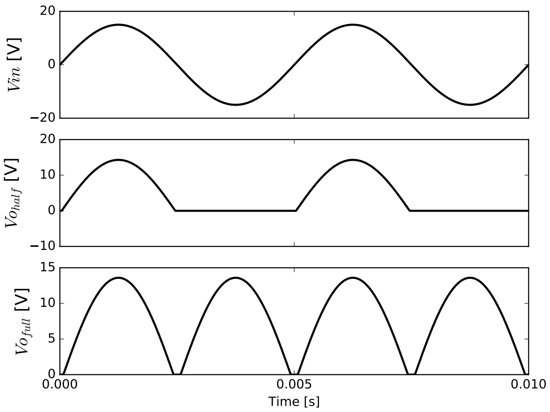

Figure 19 – Single phase half and full wave rectified outputs.

rectifier is also called diode bridge.

The following formulation is adapted from (PEJOVIC, 2007). The input voltages of a three-phase diode bridge, that are sinusoidal waves $\frac{2\pi}{3}$ out of phase, are represented by Equations (2.22) to (2.24).

$$v_1 = V_m cos(\omega_0 t) \tag{2.22}$$

$$v_2 = V_m cos(\omega_0 t - \frac{2\pi}{3}) \tag{2.23}$$

$$v_3 = V_m cos(\omega_0 t - \frac{4\pi}{3}), \tag{2.24}$$

where V_m is the phase peak voltage [V] and $\omega_0 t$ the phase of the reference phase voltage [rad].

The positive output terminal voltage v_A, that results from the operation of the diodes, will be equal to the maximum of the phase voltages. Similarly the negative output terminal voltage v_B will be equal to the minimum of the phase voltages:

$$v_A = max(v_1, v_2, v_3) \tag{2.25}$$

$$v_B = min(v_1, v_2, v_3) \tag{2.26}$$

The output voltage of a three-phase diode bridge rectifier, given by Equation (2.27), is shown in Figure 20.

$$v_{OUT} = v_A - v_B \tag{2.27}$$

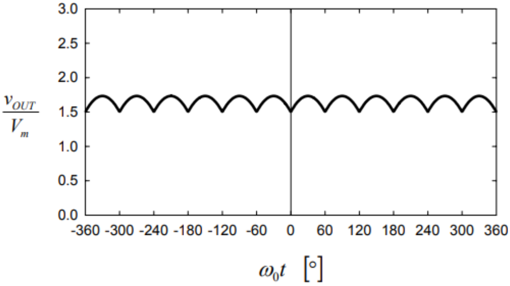

Figure 20 – Wave form of a three-phase rectified voltage.
Source: (PEJOVIC, 2007).

The DC component of the output voltage is given by Equation (2.28).

$$V_{OUT} = \frac{3\sqrt{3}}{\pi} V_m \tag{2.28}$$

The maximum reverse voltage over the diodes V_{Dmax}, given by Equation (2.29), is equal to the line voltage amplitude.

$$V_{Dmax} = V_m\sqrt{3} \tag{2.29}$$

2.4.2 Controlled Rectifiers

Controlled rectifiers can follow the same topology of the uncontrolled rectifiers, with the diodes replaced by thyristors. A thyristor is a three-terminal device that acts like a diode when the gate, its third terminal, is triggered. Such circuits are common in large-scale power systems when a conversion from alternating current into direct current is needed, sometimes reaching the scale of megawatts.

The main advantage of such systems is allowing to control output voltage and current by manipulating the thyristor gates. However, it is a more expensive and complex circuit in comparison to an equivalent uncontrolled rectifier, as it demands additional circuitry and a suitable control algorithm. Also, a thyristor is generally higher priced than a diode with the same specifications.

2.5 DC-DC CONVERTER

A DC-DC converter is a switching electronic circuit that converts energy from a DC input source to a DC output. It allows to control the output voltage by changing the duty cycle applied to the switches. The duty cycle of a periodic signal is the ratio between the period it is active and the period it is inactive and may be expressed as:

$$D = \frac{P_W}{T}, \tag{2.30}$$

where D is the Duty Cycle, P_W is the pulse width (the time that the signal is active) and T is the total period of the signal.

DC-DC converters can be divided into two groups, the isolated and the non-isolated converters. This work will focus only in the non-isolated converters, specifically the buck, boost and buck-boost converters, that are robust and simple topologies, being common choices for small wind turbine systems.

The converter most important elements are the active components, i.e. the switches, and the passive elements, i.e. the inductors and capacitors. The function of each of these elements are detailed below.

- Switch: The switches are responsible to open the circuit, interrupting the current in the circuit. Usually transistors, either Bipolar Junction Transistors (BJT) or Field-Effect Transistors

(FET), and diodes are used as a switch.

- Inductor: In switching power supplies the inductor is responsible to store energy in its magnetic field, due to the current flowing through the coil. In a practical perspective, the inductor attempts to maintain a constant current flow, limiting the rate that the current changes through time. Typically, when designing a power supply, the inductance value is chosen to limit the current ripple in order to achieve some design specification.

- Capacitor: The output capacitance is mainly used to store energy in its electric field avoiding that the voltage applied to its terminals changes drastically. The value of output capacitance is chosen to limit the output voltage ripple to some design specification level.

Several converter topologies have been developed to attend a myriad of applications in which a DC-DC converter is needed. A topology refers to the way that the active components and the passive elements are connected. Each topology has its unique properties, such as the voltage and current conversion ratios, the power loss in each component, the current and voltage ripple and its frequency response.

The most important aspects of a DC-DC converter are the static gain, that is how the duty cycle affects the ratio between the input and output voltages, and the equations that represent the system dynamics. A well known approach is to use the average model to describe the system dynamic behavior.

The characteristics of the non-isolated converters most suitable to small wind turbine systems are disposed below. The equations follows the work from (SIRA-RAMÍREZ; SILVA-ORTIGOZA, 2006) and (BARBI, 2015), that presents all the analysis needed to get the resulting equations. Knowing these characteristics allow to choose the converter topology that is more appropriated to fulfill the requirements of each project.

2.5.1 The Buck Converter

The Buck converter is well known DC-DC circuit that steps down the input voltage. The circuit, implemented with fet switches, is shown in Figure 21.

The static gain of a Buck converter is given by the following equation:

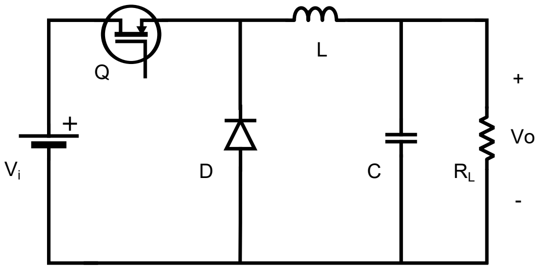

Figure 21 – Buck converter circuit.

$$V_o = DV_i \tag{2.31}$$

The average dynamic model for the Buck converter is described by Equations (2.32) and (2.33).

$$L\frac{di_L}{dt} = -v_o + Dv_i \tag{2.32}$$

$$C\frac{dv_o}{dt} = i_L - \frac{v_o}{R} \tag{2.33}$$

2.5.2 The Boost Converter

The Boost is a DC-DC converter topology that steps up the input voltage. Figure 22 shows the Boost circuit.

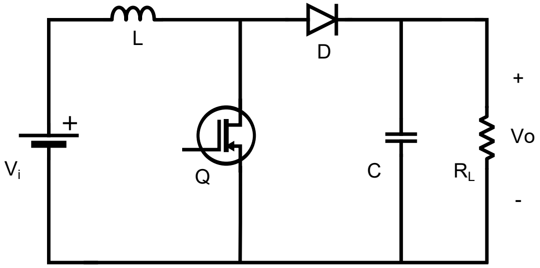

Figure 22 – Boost converter circuit.

The static gain of a Boost converter is given by:

$$V_o = \frac{V_i}{1-D} \tag{2.34}$$

The Boost converter average dynamic model is described by Equations (2.35) and (2.36).

$$L\frac{di_L}{dt} = -(1-D)v_o + v_i \tag{2.35}$$

$$C\frac{dv_o}{dt} = (1-D)i_L - \frac{v_o}{R} \tag{2.36}$$

2.5.3 The Buck-Boost Converter

The Buck-Boost converter is a DC-DC power converter, also known as chopper-amplifier converter due to its capability to work either as a step-up or a step-down converter. It is a versatile circuit, that works in a large range of operation. However, a property of this topology, undesired in many applications, is that the output voltage is of opposite sign to the input voltage.

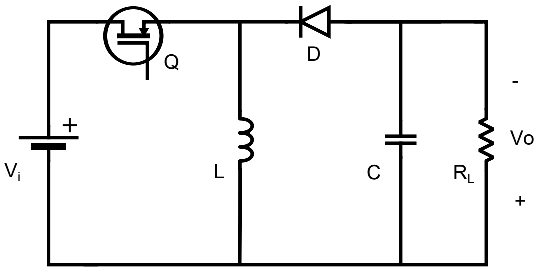

Figure 23 – Buck-boost with semiconductor switch.

The Buck-Boost static gain is given by the following expression:

$$V_o = -V_i\frac{D}{1-D} \tag{2.37}$$

Its average dynamic equations are expressed in Equations (2.38) and (2.39).

$$L\frac{di_L}{dt} = (1-D)v_o + Dv_i \tag{2.38}$$

$$C\frac{dv_o}{dt} = -(1-D)i_L - \frac{v_o}{R} \tag{2.39}$$

2.5.4 Non Inverting Buck-Boost

The Non Inverting Buck-Boost converter (NIBB) is a versatile circuit, being able to operate both as a Buck, a Boost and a Buck-Boost converter. At any operation point, the output voltage is of same sign to the input voltage, then it is a viable alternative to applications where such requirement is necessary. However, its drawback is that the topology requires more components, affecting the system efficiency and increasing the control complexity. Figure 24 shows the non inverting Buck-Boost circuit, implemented with 4 controlled switches.

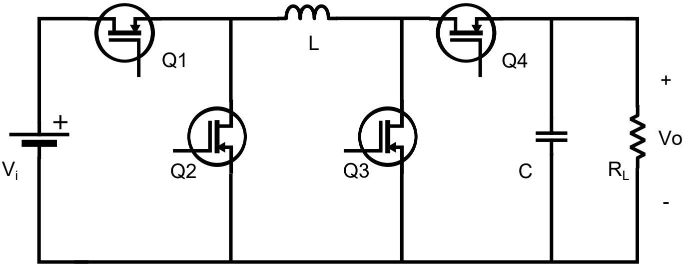

Figure 24 – 4 controlled switches NIBB circuit.

An alternative design, shown in Figure 25, replaces two controlled switches for two diodes, minimizing the control complexity.

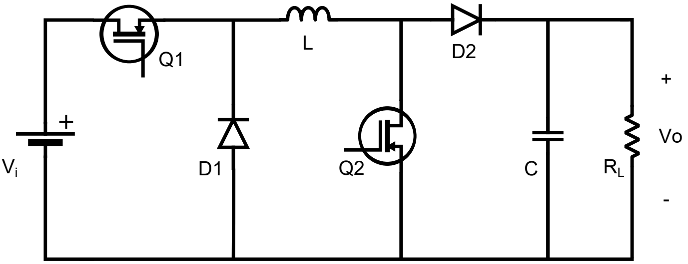

Figure 25 – NIBB circuit.

Having two switches, many switching techniques are possible for the NIBB converter. If only one of the switches is operated, the system can operate either as a buck or a boost converter. Some other methods consist in operating both switches with out-of-phase PWM signals. Usually, the control method of a NIBB converter consists in switching both switches with the same PWM signal source leading the system to operate as a buck-boost converter, being the only method covered in this work. For a system operating with such method, the static gain is given by Equation (2.40).

$$V_o = V_i \frac{D}{1-D} \tag{2.40}$$

Equations (2.41) and (2.42) describe the average model dynamics for the NIBB converter.

$$L\frac{di_L}{dt} = -(1-D)v_o + Dv_i \tag{2.41}$$

$$C\frac{dv_o}{dt} = (1-D)i_L - \frac{v_o}{R} \tag{2.42}$$

2.6 BATTERY

The use of intermittent or variable sources of energy, i.e. sources that are affected by intermittency of weather conditions or diurnal variations, sometimes becomes practical only if some means of energy storage is possible (National Academy of Sciences, 1981). A proper energy storage device allows operating an energy system based on fluctuating renewable sources in a way as stable as conventional systems. It also represents a mean to decouple the generator and its electrical production from its use, minimizing related issues between energy supply and demand (HALL; BAIN, 2008).

The most recurrent application of energy storage systems in a commercial scale has been to provide backup supply for critical loads. In micro-grid networks and stand-alone power systems, it is especially difficult to support a critical load with an intermittent power supply and having an energy storage device is of great importance in such cases (MOHOD; AWARE, 2012).

2.6.1 Definition

A battery is a device that contains chemical energy stored in its active materials and allows converting it directly into electric energy by means of an electrochemical oxidation-reduction reaction. A battery consists of one cell, which is the basic electrochemical unit, or more. The cells in a battery can be arranged in series or parallel, or even in a mix of both, depending on the desired electrical requirements. When the battery allows a reversible electrochemical reaction it is referred to as a rechargeable battery. The recharging process consists in transferring electrons from one material to another through a proper electric circuit (LINDEN, 1984).

The interest upon batteries has grown due to the broad increase in the use of battery-operated portable electronics and, more recently, emerging applications as the renewed interest in low emission vehicles and renewable energy system development. Annual battery sales more than doubled in a couple of decades, and currently are about $65 billion worldwide (PILLOT, 2015).

Different types, designs and sizes of batteries have been developed in order to attend the many applications for battery power altogether with different environmental and electrical conditions under which they must operate. Choosing the right battery leads to the most advantageous performance under each specific operational conditions, therefore knowing the characteristics of many technologies is essential for projects where a battery is needed.

In most cases it is recommended to select the battery at the beginning of the system development rather than at the end, as it can greatly affect the design of both mechanical and electrical associated systems.

2.6.2 Technologies

Many advances to improve and develop new battery technologies have been made in past years, both by discovering new battery chemistries or through the improvement of a specific electrochemical system. Nevertheless, there is still no battery that performs optimally for every application and operating conditions.

When selecting the battery the proper factors must be considered according to the system requirements for a particular application. These factors include the operating voltage, temperature requirements, environmental conditions, security and reliability, price and many other particular characteristics associated to a specific battery technology. Table 2 shows the properties of some battery technologies available in the market.

Table 2 – Comparison between rechargeable cell battery technologies.

Type	Lead-acid	NiCad	NiMh	LiCoO2	LiFePO4
Nominal Operating Voltage	2	1.2	3.7	3.7	3.3
Specific energy [$\mathrm{W\,h\,kg^{-1}}$]	33-42	40-60	60-120	250-730	90-110
Patent protection	No	No	No	No	Yes
Price	1	2	2.4	4	>10
Security	Good	Good	Good	Bad	Good
Green product	No	No	Yes	Yes	Yes
Memory effect	No	Yes	Yes	No	No
Energy efficiency [%]	60	75	70	90	95
Cycle life	400	500	500	>500	>2000
Charge time [h]	8	1.5	4	2-4	<2
Self discharge [%/month]	20	30	35	10	8

Source: (HUA; SYUE, 2010).

2.7 SENSORS

Having the right sensors is essential for most maximum power point track (MPPT) strategies. It also allows to trigger safety measures in case the system gets to a dangerous state of operation. Some of the most common sensors in wind turbine systems are:

- Anemometer: Used to measure the wind velocity. The cup shaped anemometer is the most popular format. This system consists in three cups attached to a shaft with a vertical axis of rotation. The output signal can be a AC sine wave, with the wave frequency proportional to the wind speed, or a DC signal, with its amplitude proportional to the wind speed. Wind measurement is important in MPPT strategies that depend on the tip speed ratio. Also, if the wind velocity surpasses the established maximum safe value, some security measure can be triggered to protect the system.

- Tachometer: This device gives information above the angular velocity of the main shaft and is important to compute the tip speed ratio. Hall effect sensors that are embedded in some generators can be used, but a sensorless alternative that consists in estimating the rotational speed using the back-EMF frequency is also possible. Sometimes the rotational speed is obtained through the information given by an encoder, by computing the angular position derivative.

- Voltage and current measurement: Measuring the output voltage and current of a wind turbine is important to determine the electric output power of the system. These measurements are also related to the mechanical variables of the generator (rotation speed and torque). Furthermore, in order to avoid exceeding the operational limits of additional elements connected to the generator, as the DC-DC converter, the battery or even the load, it is essential to constantly observe the electrical quantities and apply some measure when the system reaches a risky operation point.

- Other sensors: A temperature sensor, barometric pressure sensor, and solar radiation sensor may be added to the system, although they are rarely assembled into small scale systems. The temperature and pressure sensors allow to accurately compute the air density. Measuring the temperature is also important as high temperatures can affect electronic devices and damage the battery.

2.8 MPPT

In a variable source power system, tracking the maximum power point is essential to optimize the power generation. As shown in Equation (2.10), the power coefficient C_p, therefore the mechanical power itself, is a function of the tip-speed ratio and the blade pitch angle. For a small wind turbine the pitch is usually fixed, therefore the extracted power from the wind depends only on the tip-speed ratio, or the rotational speed for a given wind speed.

Knowing that in a permanent magnet synchronous generator the output voltage is proportional to the rotor speed, the MPPT control of a fixed pitch rotor system consists in controlling the output voltage of the generator by regulating the DC-DC converter duty cycle (MAHDAVIAN et al., 2014).

2.8.1 Optimal tip-speed ratio control

The optimal tip-speed ratio control (OTSR) consists in controlling the generator rotational speed in order to achieve the optimal tip-speed ratio for a measured wind speed. Having the model of the wind turbine, described by a curve similar to Figure 14, it is possible to determine the tip-speed ratio that maximizes the output power.

With the desired tip-speed ratio, λ_{opt}, and the measure of the wind velocity it is possible to compute the optimal rotational speed, ω_{opt}, by manipulating Equation (2.9):

$$\lambda_{opt} = \frac{\omega_{opt} \cdot R_b}{V_w}$$

$$\omega_{opt} = \frac{\lambda_{opt} \cdot V_w}{R_b} \tag{2.43}$$

Figure 26 shows the OTSR method represented as a block diagram.

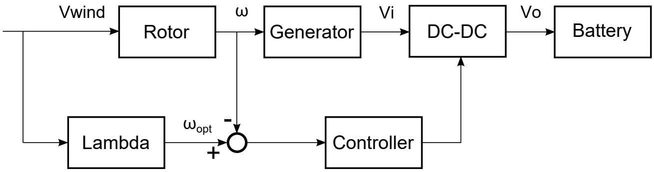

Figure 26 – Tip-speed ratio MPPT diagram.

OTSR is a method easy to understand and implement, but one of its disadvantages is that it requires the wind turbine characteristics and both wind speed and rotational speed measurement. To overcome the need of a mechanical shaft speed measurement, it can be estimated through the line voltage frequency of the wind turbine.

2.8.2 Power Signal Feedback

Power Signal Feedback (PSF) is a MPPT method that uses the wind turbine rotational speed to calculate the optimum power. Then a current reference is computed by dividing the expected output optimum power by the rectified voltage.

The optimum power is obtained through an equation that describes the MPP as a function of the rotational speed, usually a cubic curve, that can be fitted either by an experimental or theoretical model of the system (FARIAS et al., 2017). Alternatively, these data can be used to create a table with the rotational speeds and maximum output power and then the optimum power is obtained simply by finding the correspondent rotation velocity in the table.

The optimal mechanical power generated by the turbine is defined by Equation (2.44).

$$P_{m_{opt}} = K_{opt} * \omega_m^3, \tag{2.44}$$

in which K_{opt} is the parameter to be fitted, that defines the optimal power curve, ω_m is the generator rotational speed and $P_{m_{opt}}$ is the optimum mechanical power.

Usually a wind turbine model, such as given by Equation (2.10), refers to the mechanical power extracted from wind. However, it is easier to measure and control the system electrical output power. The electrical optimal power $P_{e_{opt}}$ can be derived from $P_{m_{opt}}$ by considering all electrical losses in the system, represented as η. Then, the resulting equation is given by:

$$P_{e_{opt}} = \eta P_{m_{opt}} \tag{2.45}$$

Figure 27 shows how a cubic curve can approximate the MPP of a small wind turbine with the parameters from Table 1.

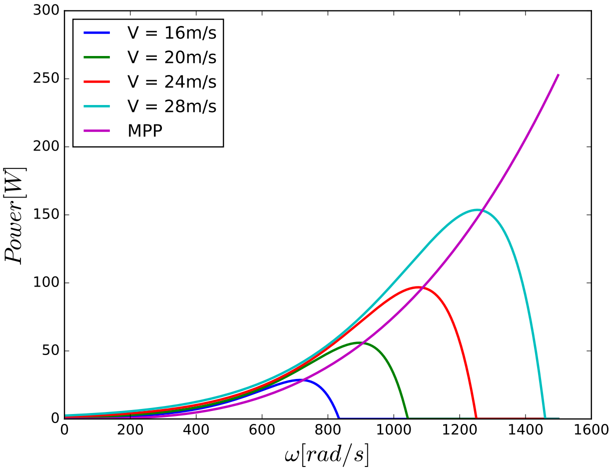

Figure 27 – Cubic curve fitted to small wind turbine power curves.

The PSF workflow consists in measuring the rotational speed, then Equation (2.45) is used to compute the MPP. With the expected maximum power for the measured rotation, a current reference is obtained by dividing the expected power by the measured rectified voltage as shown in Equation (2.46).

$$i_{ref} = \frac{P_{e_{opt}}}{V_{cc}} \tag{2.46}$$

With the current reference computed, a closed-loop control system is used to make the system achieve the MPP. A block diagram representing the PSF method is shown in Figure 28.

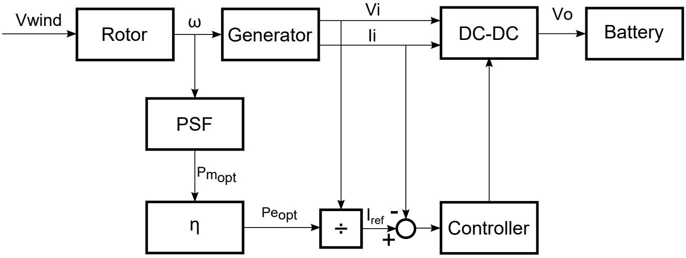

Figure 28 – Power Signal Feedback MPPT diagram.

The PSF method requires less mechanical sensors than OTSR, because it is independent of the wind velocity measurement. However, measuring both output current and rectified voltage is necessary. Measuring the rotational speed is also needed. A speed-sensorless PSF can be implemented by estimating the rotational speed with the line voltage frequency. Like in OTSR, a proper model of the wind turbine is necessary, in order to obtain the maximum power curves of the wind turbine.

When using a BLDC machine with a rectifier, it is also possible to fit a cubic curve for the MPP as a function of the rectified voltage, that is somehow proportional to the rotational speed. The MPP as a cubic function of the rectified voltage is given by Equation (2.47). Nonetheless, the data required to model the output power as a function of the voltage is hard to be obtained theoretically, because the models for the generator and the rectifier are way complex. The usual is to acquire the data through simulations or experiments.

$$P_{e_{opt}} = K_V * V_{cc}^3 \tag{2.47}$$

2.8.3 Perturbation and Observation

Perturbation and observation method (P&O) is a hill climbing algorithm that consists in perturbing the rotor speed to compare the present turbine output power with the past value. If the output power increases, the controller continues to perturb the system in the same direction; otherwise the system is perturbed in the opposite direction (ELGENDY, 2016). A flowchart representing the P&O algorithm is disposed in Figure 29.

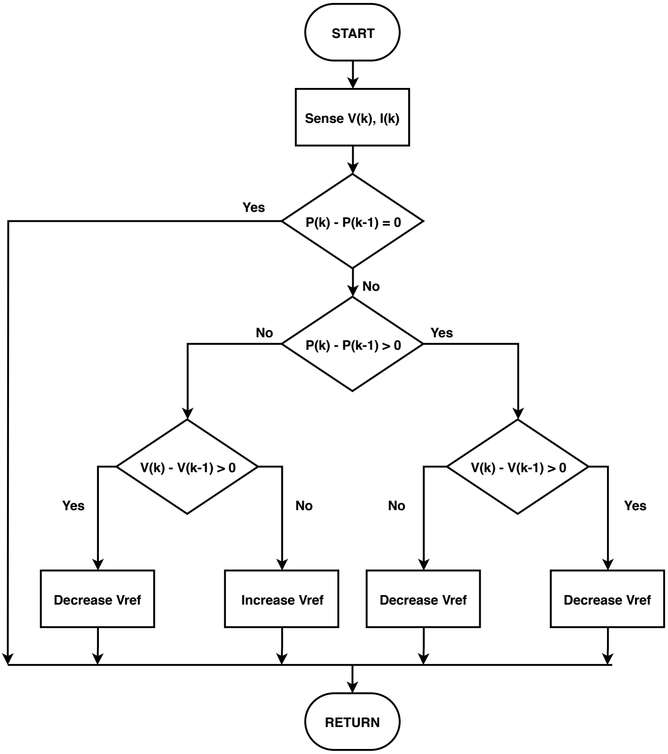

Figure 29 – P&O algorithm flowchart.

P&O is a popular method since it is a low complexity algorithm, not requiring the knowledge of system specifications, and it is a low cost strategy, since it does not require a sensor to measure the wind speed and the shaft rotational speed. However, measuring the output power is necessary. Usually this is done by measuring the electrical variables in the DC-DC converter, *i.e.* its output current and voltage. It is important to notice that P&O presents oscillations in the output power even after achieving the MPP.

2.9 ADDITIONAL COMPONENTS

Some additional components may be necessary in a wind power system, but are less common in small-scale systems for presenting an elevated cost and not increasing significantly the efficiency in such small devices. Some of the most important components are:

- Gearbox: it is an element situated between the rotor and the generator, responsible to adequate the angular velocity to the generator specifications. In a large wind turbine the rotor angular velocity can be as slow as 15 RPM, while the generator is usually designed to work with a speed near 1800 RPM.
- Brake system: two methods can be used to brake a wind turbine, a measure commonly used upon extreme wind conditions to prevent the rotor to spin way too fast or when some maintenance service is required. The first one is the electrical braking system, that consists in using a resistor bank to convert the kinetic energy of the turbine into heat. The other method is a mechanical braking, that uses a drum or disk brake to stop the turbine. In large turbines the two methods can be used altogether, with the mechanical brakes being applied after the rotation is slowed down by the electrical brake, to avoid the huge momentum to break or even create fire if the mechanical brake is used with the turbine at full speed.
- Yaw motor and driver: In large wind turbines a system to actively control the position of the turbine in order to align the nacelle to follow changes in wind direction and optimize the power generation can be present. In small turbine systems a tail vane can be used to orient the rotor using the force of the wind itself.

3 DESIGN

With the theoretical knowledge about wind turbine systems already presented in Chapter 2, each element of the project can be properly designed. This chapter begins with a new mechanical design proposition for the control pod, with the features necessary to fly along with the kite system. Afterwards, the turbine rotor design is presented, followed by the generator chosen to attend the requirements for this project. In the sequence, the designed circuits for the rectifier and the DC-DC converter, along with chosen components and designed circuit boards are shown. Then, the battery pack design is presented. The chapter ends with the design of a data acquisition system, that is necessary to collect the experimental data, and the design of a case to stabilize the wind turbine system during the wind tunnel experiments.

3.1 CONTROL POD MECHANICAL DESIGN

The control pod is the unit that carries all the elements necessary to control the flight trajectory of the AWE pumping kite system. To attach the micro wind turbine to it a proper mechanical design must be developed. It is important to notice that the control pod will fly near the airfoil, adding extra drag and weight, leading to a reduction in the total efficiency and affecting the kite flight dynamics. Therefore, minimizing the dimensions and weight of the control pod and working on its aerodynamics must be the aims of its design project. Furthermore, some security concerns must be taken into consideration as it is a solid and heavy unit that can fall from hundreds of meters if something goes wrong with the AWE operation.

The proposed design follows the shape of an usual airplane wing, with its front-face shaped in a way that minimizes the drag force and forces it to be always aligned with the wind, letting the air go through the wind turbine at the higher possible speed.

Considering that the wind turbine is designed to operate at a high rotational speed, a well-designed coupling between the control pod and the wind turbine is critical. It was chosen to place the wind turbine in a compartment inside the control pod. This is a safer alternative because even if some component dismantles from the turbine, it will be confined inside the compartment, preventing it from falling apart. This concern is also applied to the other elements that are placed inside the control pod. The most delicate device is the battery, as several chemical technologies present a risk to ignite fire. To avoid potential incidents the battery should be in an individual compartment separated from the other elements. Figure 30 shows the control pod proposed design.

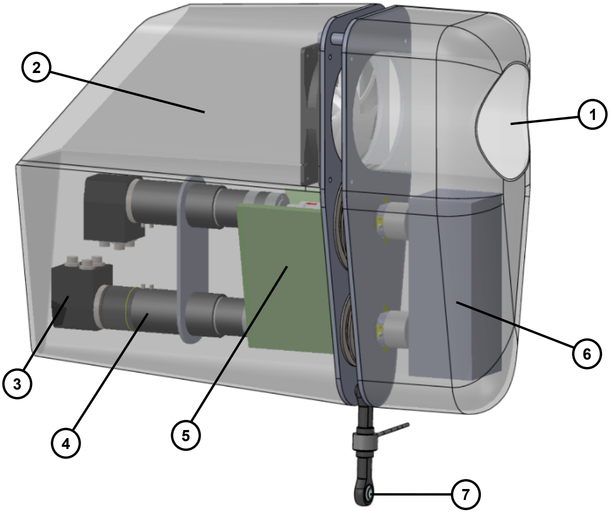

Figure 30 – Proposed new control pod design. ① air entrance, ② wind turbine rotor and generator compartment, ③ encoders, ④ motors, ⑤ electronic devices compartment, ⑥ battery and ⑦ traction tether holder.

3.2 ROTOR

Designing a proper rotor was a difficult task in this project due to the fact that it is uncommon to design a wind turbine system with such reduced dimensions and that it is intended to operate at that high altitude and wind velocity. The desired maximum diameter for the rotor is of 20 cm, in order to fit inside the designed control pod.

The first attempt was to use commercial propellers for radio controlled airplanes and drones. It was a convenient choice as there are numerous types and models largely available. However, the initial results, acquired by tests performed in a wind tunnel, showed that these propellers have an efficiency way bellow the desired for this project. Even a 10x5 propeller, with a diameter of 10 inches (25.6 cm), presented an output power bellow what was expected. It became clear that using such propellers would lead to a rotor larger than desired. Figure 31 shows the 10x5 propeller used in the first tests.

Figure 31 – 10x5 propeller.
Source: Hobby King catalog, available in `https://hobbyking.com`.

A second prototype was designed using blades available to purchase separately. 70 mm length blades were chosen, meeting the maximum size constraint. A hub, responsible to hold the blades together and attach the rotor into the shaft of the generator, must be designed and manufactured.

A prototype was designed to work with the chosen blades and manufactured using aluminum. Aluminum was chosen because it is a resistant material, lighter then steel and easy to work with the available tools. The designed rotor hub consists in two pieces united by bolts that must be evenly tightened to prevent the blades from moving during the flight.

Figure 32 shows the rotor prototype, with the blades mounted into the hub. The option of printing the piece in a 3D printer was discarded due to the need of a resistant material, regarding mostly to the bolt threads, in order to avoid the hub to slip out the shaft while rotating at a high speed.

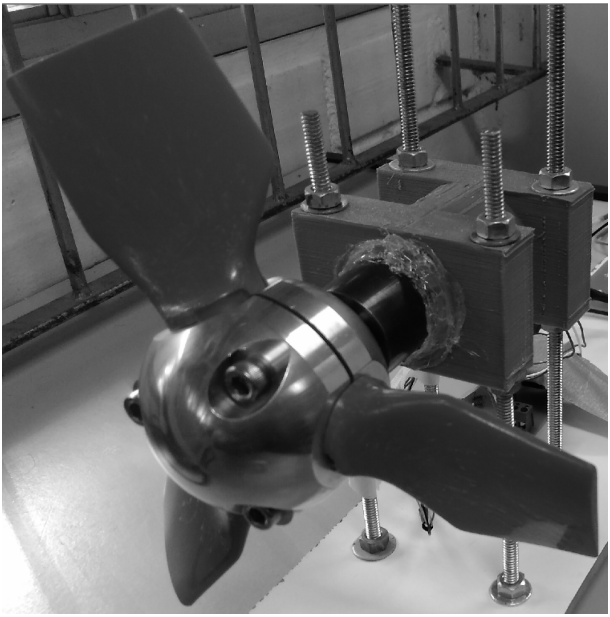

Figure 32 – New rotor design.

The prototype performed well in the preliminary tests. However, for being too heavy, it is suitable only to be used in wind tunnel tests. The mass of the rotor elements, measured with a precision scale, are disposed in Table 3. After the validation of this rotor design, the hub can be manufactured in plastic by using injection moulding or other similar method. As an example, a hub made of High Density Polyethylene (HDPE) would reduce the rotor hub mass in 65 %.

Table 3 – Designed rotor components mass.

Component	Mass [g]
Bolts (x3)	5
Blade (each)	30
Hub	295
Total	390

3.3 GENERATOR

In this project the principal generator characteristic to be achieved is to have a high power density, allowing to minimize its size and weight. Also, it must support a great rotational speed in order to work with the high expected wind velocity. The rotational speed can only be accurately determined after the wind turbine rotor is designed and modeled, but an initial guess is that the system must support at least 15,000 RPM. Also, the generator must be capable to supply at least 100 W, giving a good margin over the 60 W average power that the system is designed to provide.

The chosen generator was the BLDC machine shown in Figure 33. It is a high performance slotless brushless precision motor with an efficiency up to 94%. Its applications are mainly aerospace, military, electric power tools, medical, and industrial. Constructively it is a 4 pole slotless machine, with great power density, high continuous and peak torque, low inerti8a and small inductance. It uses low loss lamination materials for maximum performance.

The specifications for the chosen machine, given by the manufacturer, are disposed in Table 4.

Figure 33 – Chosen BLDC machine.

3.4 RECTIFIER

Designing a rectifier consists in choosing the topology and dimensioning its components. As shown in Section 2.4, the most adequate topology for this project is a full-wave uncontrolled rectifier, a three-phase diode bridge, because the supplementary circuitry necessary to

Table 4 – BLDC generator specifications.

Nominal voltage [V]	48
Nominal power [W]	430
No load speed [RPM]	$19,756$
Winding resistance [Ω]	0.285
Winding inductance [mH]	0.11
Maximum efficiency [%]	94
Static friction [oz-in]	0.20
Damping factor [oz-in/RPM]	0.013
Rotor inertia [10^{-4}oz-in-sec^2]	3.9

control a thyristor based rectifier does not worth the additional gain in efficiency, that is minimal for such small associated power.

Commonly a bridge rectifier is chosen regarding the average rectified current and the maximum reverse blocking voltage. Knowing that the system is designed to produce an average power of 60W, it is possible to extrapolate this value to calculate a maximum expected rectified current I_{max}. It will be considered that the wind turbine generates a maximum power, P_{max}, of 100W, with a rectified voltage, V_{rec} of 25V, that is below the generator nominal voltage given by Table 4. Those values give a fair margin to exceed the output current requirement.

$$I_{max} = \frac{P_{max}}{V_{rec}} \tag{3.1}$$

$$I_{max} = \frac{100}{25} \tag{3.2}$$

$$I_{max} = 4A \tag{3.3}$$

In order to calculate the maximum reverse voltage, firstly the expected phase peak voltage, V_m, is determined by the manipulation of Equation (2.28). It will be considered that the output DC voltage is the nominal voltage of the generator, available in Table 4.

$$V_m = \pi \frac{V_{OUT}}{3\sqrt{3}} \tag{3.4}$$

$$V_m = \pi \frac{48}{3\sqrt{3}} \tag{3.5}$$

$$V_m = 29.02V \tag{3.6}$$

Then the diodes maximum reverse voltage is given by Equation (2.29).

$$V_{Dmax} = 29.02\sqrt{3} \tag{3.7}$$

$$V_{Dmax} = 50.26V \tag{3.8}$$

Based on the maximum electrical results, the VS-36MT160 bridge from Vishay Semiconductors© was chosen. It is a bridge that surpasses by far the electrical requirements, but was already available in the laboratory. Choosing an integrated circuit instead of a discrete bridge simplifies the mounting and eventual replacement in case of failure. VS-36MT160 specifications are available in Table 5.

Table 5 – VS-36MT160 specifications.

Maximum DC output current [A]	35
Maximum repetitive peak reverse voltage [V]	1600
Threshold voltage [V]	0.86
Slope resistance [Ω]	6.3
RMS isolation voltage [V]	2700
Maximum temperature range [°C]	-55 to 150

Source: (VISHAY, 2017).

3.4.1 Printed Circuit Board

With the rectifier components chosen the printed circuit board (PCB) can be also designed. This circuit is responsible for the interface between the generator and the converter, then the same PCB will be used to host the rectifier also to route the hall sensor connections.

The circuit, shown in Figure 34, has two separated ground planes with a jumper to connect them if desired. Sometimes it is good practice to separate power and signal planes to protect the low voltage components from some electrical discharge or interference from the power devices. Although the generator output voltage is not supposed to be very high, it is good to have the option to decouple both circuits. A pull-up resistor is connected to each Hall sensor channel, as suggested by the manufacturer. The capacitive filter, that consists in a 1000 µF 50 V capacitor, is placed after the diode bridge. Also, two indicative LEDs were added to the circuit. The first shows that the Hall sensor is connected to the 5 V power supply while the other is powered by the rectified voltage, indicating that the rotor is spinning and the generator is able to produce energy. Those LEDs are optional, designed to facilitate the experiments.

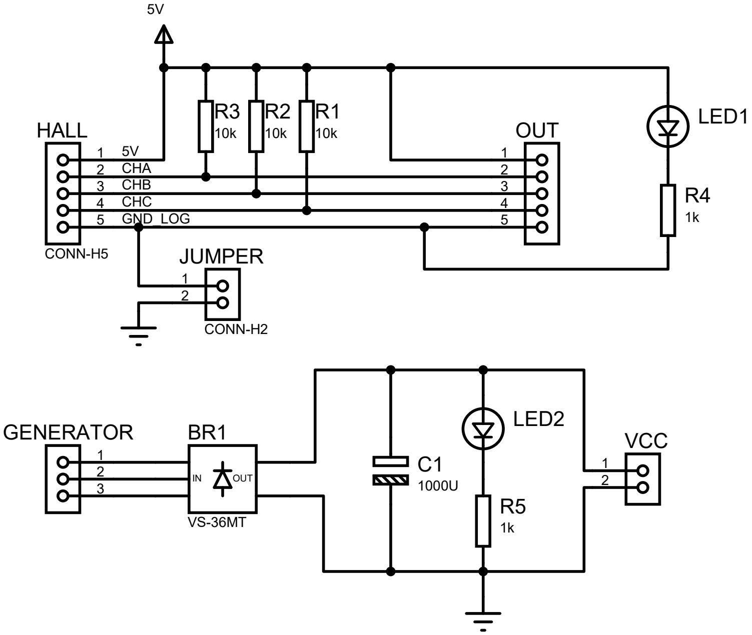

Figure 34 – Rectifier and Hall sensor routing circuit schematic.

Subsequently the PCB layout was designed. Figure 35(a) shows the layout displaying also the silk layer, that represents the placement of each component. In Figure 35(b) just the PCB layout is shown. The ground planes are visually separated and united by a single jumper.

3.5 DC-DC CONVERTER

The DC-DC converter chosen topology was the non-inverting Buck-Boost. It can either step-up or step-down the rectified voltage, making it a more versatile converter. Considering that the converter was designed before modeling the rotor and generator to determine the

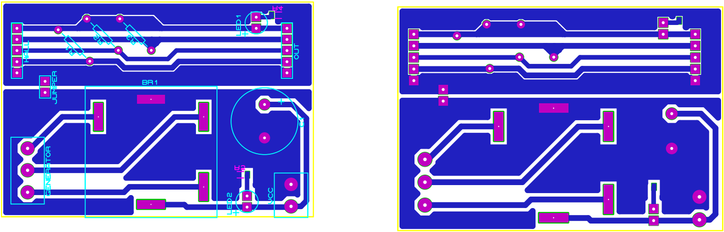

(a) PCB design.

(b) Layout.

Figure 35 – Rectifier circuit PCB design.

turbine output voltage for the desired wind speed range, this is a more suitable choice.

The design of this switched converter consists in choosing the switches and determining the values for the capacitor and the inductor to fulfill the project requirements. The most important parameters to be determined are the output voltage and current, that results in the output power. The switching frequency is also an important parameter, but usually it is limited by the hardware used to control the electronic switches and the switch technology.

For this project, the nominal output voltage is given by the battery voltage. The output current can be computed by dividing the desired system output power by the output voltage. The maximum input voltage is the generator nominal voltage, from Table 4. The minimum voltage is chosen to allow the system to work in a wide range of operation. It is also important to determine a acceptable maximum ripple in the current and voltage signals. Table 6 summarizes the specifications for the designed converter.

Table 6 – Non inverting Buck-Boost design specifications.

V_o	Output voltage	24 V
I_o	Output current	2.5 A
$V_{i_{min}}$	Minimum input voltage	10 V
$V_{i_{max}}$	Maximum input voltage	48 V
F_{sw}	Switching frequency	20 000 Hz
$\Delta I_{\%}$	Current percentage ripple	10 %
$\Delta V_{\%}$	Voltage percentage ripple	1 %

The input and output voltages can be used to determine the duty cycle range of operation. This is important because surpassing those values leads the power supply to an undesired operation mode that can potentially damage some component. Knowing that the output voltage is constant, the minimum and maximum values of the non-inverting buck-boost can be given by:

$$D_{min} = \frac{V_o}{V_{i_{max}} + V_o} \tag{3.9}$$

$$D_{min} = 0.333 \tag{3.10}$$

$$D_{max} = \frac{V_o}{V_{i_{min}} + V_o} \tag{3.11}$$

$$D_{max} = 0.706 \tag{3.12}$$

The absolute value for both current and voltage output peak-to-peak ripple is given by:

$$\Delta V = V_o \cdot \Delta V_{\%} \tag{3.13}$$

$$\Delta V = 0.24\,\mathrm{V} \tag{3.14}$$

$$\Delta I = I_o \cdot \Delta I_{\%} \tag{3.15}$$

$$\Delta I = 0.25\,\mathrm{A} \tag{3.16}$$

The inductor current ripple is proportional to the average applied voltage and inversely proportional to its inductance and the switching frequency. Thus, the following equation can be used to compute the inductance:

$$L = V_o \cdot \frac{1 - Dmin}{\Delta I \cdot f_s} \tag{3.17}$$

$$L = 2.133\,\mathrm{mH} \tag{3.18}$$

The series impedance of the capacitor and the power stage output current determine the output voltage ripple. To fulfill the voltage ripple specification, the capacitor value can be selected by using the following formula:

$$C = I_o \frac{D_{max}}{\Delta V \cdot f_s} \tag{3.19}$$

$$C = 245\,\mu\mathrm{F} \tag{3.20}$$

To choose the capacitor voltage, the maximum output voltage can be computed:

$$V_{o_{max}} = Vo + \frac{\Delta V}{2} \tag{3.21}$$

$$V_{o_{max}} = 24.12V \tag{3.22}$$

The voltage across the switches Q1 and Q2 are V_i and V_o respectively. Then the maximum voltage for the switches are:

$$V_{Q1_{max}} = V_{i_{max}} = 48V \tag{3.23}$$

$$V_{Q2_{max}} = Vo = 24V \tag{3.24}$$

The diodes D1 and D2 reverse voltage are also V_i and V_o respectively:

$$V_{D1_{max}} = 48V \tag{3.25}$$

$$V_{D2_{max}} = 24V \tag{3.26}$$

The current peak for both switches and diodes Q1, Q2, D1 and D2 is given by:

$$I_p = I_o\left(\frac{1}{1-D}\right) + \frac{\Delta I}{2} \tag{3.27}$$

And the maximum current peak will be:

$$I_{p_{max}} = I_o\left(\frac{1}{1-D_{max}}\right) + \frac{\Delta I}{2} \tag{3.28}$$

$$I_{p_{max}} = 2.625\,\mathrm{A} \tag{3.29}$$

With all the specifications and maximum ratings, it is possible to choose the converter components. For the capacitor it is important to approximate the results to standard values, that are the values of commercial components largely available. The switches and diodes must fulfill the specifications but the price and availability are also important factors. Table 7 shows the chosen components for the designed converter.

An inductor with the desired specifications was not available, then an inductor to attend this project requirements was designed and manufactured. The inductor design is described in Appendix A.

Table 7 – Non inverting Buck-Boost components.

Capacitor	330 µF, 35 V
Inductor	2.13 mH, 3 A
Switches Q1, Q2	MOSFET IRF640
Diodes D1, D2	MUR820

3.5.1 Printed Circuit Board

Developing the PCB design is the last step in the converter design. It was chosen to make two separated boards, one for the converter and another for the transistor drives, allowing to reuse the converter circuit if some modification in the drive circuit is intended. The converter circuit schematic is shown in Figure 36 and its PCB design and layout are shown respectively in Figures 37(a) and 37(b).

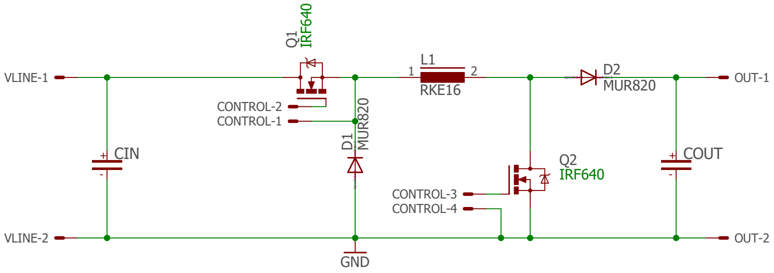

Figure 36 – NIBB converter circuit schematic.

In order to switch a MOSFET, the gate-source voltage, V_{GS}, must surpass the threshold voltage established by the manufacturer, that usually varies from 4 V to 6 V, or 8 V to 12 V in devices based in older technologies. Using a driver IC (integrated circuit) allows to convert a TTL (transistor-transistor logic) PWM signal into a voltage and current level suited to drive the MOSFETs.

The TC4422 IC driver was chosen to drive the switch Q2. It is a 9 A high-speed MOSFET and IGBT (insulated-gate bipolar transistor) driver. Considering that the Q1 source reference is not the common circuit ground, an isolated driver was chosen to guarantee the MOSFET switching. The chosen IC is the ADuM3220, a 4 A isolated driver,

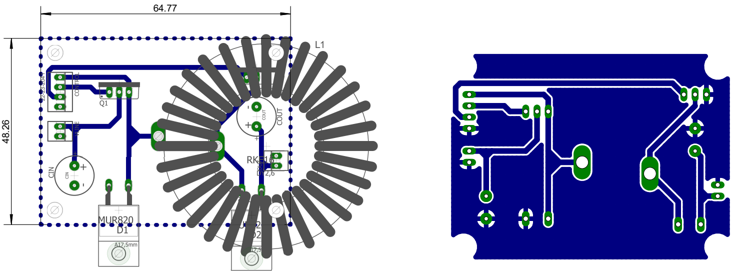

(a) PCB design. Dimensions in mm.

(b) Layout.

Figure 37 – NIBB converter PCB design.

sourced by a B1209LT-2W isolated DC-DC converter IC. A L7812 12 V linear voltage regulator is placed in the board input, preventing that the wind turbine output voltage damages some component when exceeding its maximum input voltage.

The driver circuit schematic is shown in Figure 38. The driver PCB design and layout are shown respectively in Figures 39(a) and 39(b).

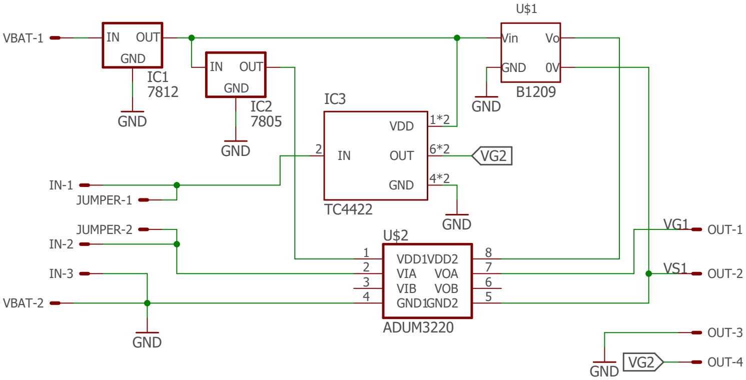

Figure 38 – NIBB driver circuit schematic.

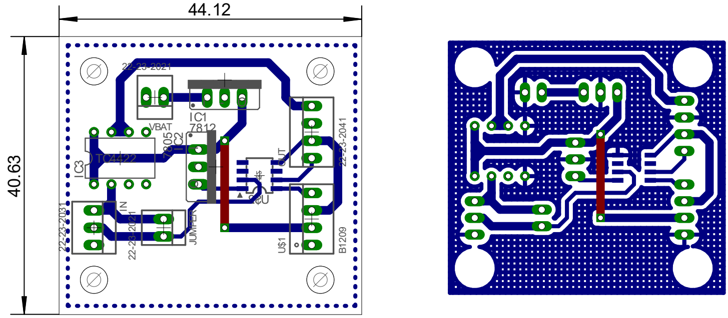

(a) PCB design. Dimensions in mm.

(b) Layout.

Figure 39 – NIBB driver PCB design.

3.6 BATTERY

Choosing the right battery consists in taking into account the several characteristics presented in Section 2.6. For the present project, the principal aspects to be optimized are:

- High specific energy: the weight and the dimensions of the battery pack must be minimized, to fit in the control pod desired dimension limits and avoid increasing its weight.
- Safety: there is a risk of impacts when the kite make some abrupt movement during its trajectory, then the battery pack must have a safety level as high as possible. Furthermore, the battery will be confined in a closed compartment within the control pod, then a technology with the least ignition risk must be selected.

Besides that, some other technical requirements where established in order to attend the electrical demands from the control pod embedded hardware. Such requirements are presented in Table 8.

Lead-acid batteries are easy to find, cheap and have a good security level, but its low specific energy would lead to an over-weighted pack. To minimize the weight it is necessary to use a Lithium based technology. The popular Li-ion batteries have a high chance of incinerating with the increase of the temperature, then it cannot be chosen either. Among the technologies presented in Table 2, the Lithium Iron Phosphate (LiFePO4) is the better choice, having a good specific energy and security level, despite being the most expensive technology.

Table 8 – Battery electrical requirements.

Nominal voltage	24 V
Capacity	$\geq$ 2.5 A h
Maximum discharge current	$\geq$ 20 A
Nominal discharge current	2.5 A
Maximum charge current	$\geq$ 10 A

Besides that, LiFePO4 batteries have a incredibly high charging cycle life, decreasing the frequency of maintenance.

The chosen battery model is the ANR26650M1B from A123 Systems©. Figure 40 shows the battery and Table 9 its specifications. To achieve the desired nominal voltage, it is necessary to build a pack with 7 cells mounted in series.

Figure 40 – ANR26650M1B battery cell.
Source: (A123 SYSTEMS, 2012).

Table 9 – ANR26650M1B battery specifications.

Voltage (Nominal / Maximum)	3.3V / 3.6V
Capacity (Nominal / Minimum)	2.5Ah / 2.4Ah
Maximum discharge current	50 A
Charging cycles	$\geq$ 1000 cycles
Weight	76 g
Cell dimensions	$\varnothing$26 mm $\times$ 65 mm

Source: (A123 SYSTEMS, 2012).

The manufacturer recommends to use the CCCV as the standard method to charge the battery, with a constant current of 2.5 A and a constant voltage of 3.6 V per cell. With the designed pack of 7 cells arranged in series, the charging current remains the same and the total constant voltage of 25.2 V.

3.7 DATA ACQUISITION BOARD

To acquire the relevant data during the experimental tests a data acquisition system (DAQ) is needed. To minimize the number of the developed circuits the same processing unit can be used to control the DC-DC converter switches. The measurement and control requirements are:

- Voltage measurement: The most important voltage signals to be measured are the rectified voltage, V_{cc}, and the battery voltage, that are respectively the input and output voltages of the converter. To cover the expected range, the system must be able to measure positive voltages up to 50 V.

- Current measurement: Measuring the converter input and output currents is important to compute the wind turbine output power and the converter output power. Such values can be used to compute the converter efficiency. Also, measuring the battery current is important to determine the SOC and to follow charging patterns indicated by the manufacturer. Both sensors must have a range of 0 A to 5 A, giving a good margin to the expected maximum output current.

- External interrupt: To compute the generator rotational speed, the microcontroller must support external interrupts in order to count the Hall sensor ticks. The signal is TTL, varying from 0 V to 5 V.

- PWM: In order to control the DC-DC converter switches, the device must support a TTL switching frequency of at least 20 kHz.

- Serial communication: Having a USART or USB port in necessary to communicate with the computer.

Using an Arduino to implement the measurement is a low-cost and functional alternative. For requiring few input and output pins, an Arduino Nano is sufficient to fulfill the requirements. Based on the ATmega328, it has 7 analog inputs, 6 PWM available outputs and an USB connector that communicates with the computer by emulating a serial port. Using the 8-bit timers (Timer0 and Timer2) based PWM pins it is possible to reach up to 62.5 kHz with the full resolution of 256 bits (ATMEL, 2011). Moreover, 2 external interrupt pins are available, allowing to use channels A and B from the Hall sensor.

The most simple alternative to measure the voltage is to use a voltage divider avoiding the signal to surpass the Arduino analog input limit of 5 V. The voltage divider circuit is represented in Figure 41, and its output voltage, V_o, is given by Equation (3.30). A 5.1 V Zener diode was added to protect the Arduino analog inputs. If a better protection circuit is needed, the Zener diode can be replaced by a clamping IC, such as the TL7726.

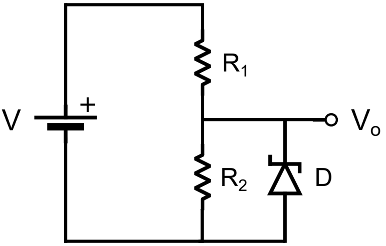

Figure 41 – Voltage divider circuit.

$$V_o = V\frac{R_1}{R_1 + R_2} \tag{3.30}$$

Choosing R_1 and R_2 resistors as 10 kΩ and 100 kΩ respectively, the maximum output voltage, with a 50 V input source, is 4.54 V, below the maximum Arduino supported voltage. The ideal is to use resistors with a tolerance below 1 %, resulting in more accurate measurements. With the Arduino 1024 bits analog ports and this voltage divider the system will have a resolution of 6 mV.

To achieve the current measurement the ACS712 module was chosen. It is a low-cost Hall- effect based current measurement circuit, compatible with the Arduino and is available in 3 current ranges: ±5 A, ±20 A and ±30 A. The ±5 A device is the most suited for this application, with a sensitivity of 185 mV A^{-1} (ALLEGRO, 2017).

The circuit connection schema is available in Appendix B.

3.8 WIND TURBINE CASE

In order to encapsulate and fix the wind turbine during the wind tunnel experiments, a case was designed and 3D printed using ABS plastic (Acrylonitrile butadiene styrene). The designed 3D model is shown in Figure 42. The case consists of a cylinder with its inner diameter equal to the generator diameter and two rectangular supports. The generator is locked into the case with the use of 2 bolts that must reach the threaded holes located in the generator base. The case is fixed by using 4 threaded rods and a set of nuts, that must be tighten to make the system steady.

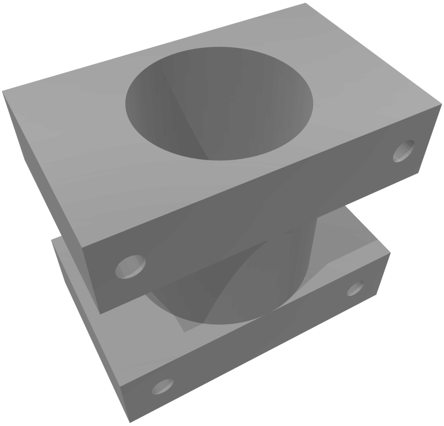

Figure 42 – Wind turbine case design.

4 MODELING AND SIMULATION

The focus of this chapter is to obtain proper models to represent the components of the designed wind turbine. This allows to simulate the system, analyze its behavior and evaluate its performance under the desired operating conditions.

The wind tunnel used for the experiments is located in Polo - UFSC, the Research Laboratories for Emerging Technologies in Cooling and Thermophysics, with a maximum volumetric air flow rate of $500\,\mathrm{m\,h^{-3}}$. Its test section has a cross section of $450\,\mathrm{mm} \times 350\,\mathrm{mm}$. To achieve the desired wind speed range, the cross section was reduced to a circumference with a diameter of $\varnothing 300\,\mathrm{mm}$.

4.1 ROTOR MODEL

An ideal approach to properly model the designed rotor is to conduct tests in a wind tunnel. Knowing that measuring the mechanical torque in the shaft is a complex task, usually the experimental output power is computed with the generator rectified voltage and load current measures.

The system to be submitted to the wind tunnel uses the designed components described in the previous with a resistive load. Then the system used to obtain the experimental data, represented in Figure 43, is composed by the rotor, the BLDC generator, the diode bridge rectifier, a capacitive filter and the resistive load.

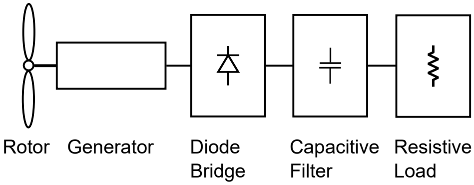

Figure 43 – System configuration for the wind tunnel test.

Firstly it is necessary to submit the wind turbine to a known wind velocity. Then, to determine the output power measurements of the load current and voltage are made and the power is computed for each wind velocity input. Figure 44 shows the wind turbine system mounted inside the wind tunnel during one of the tests.

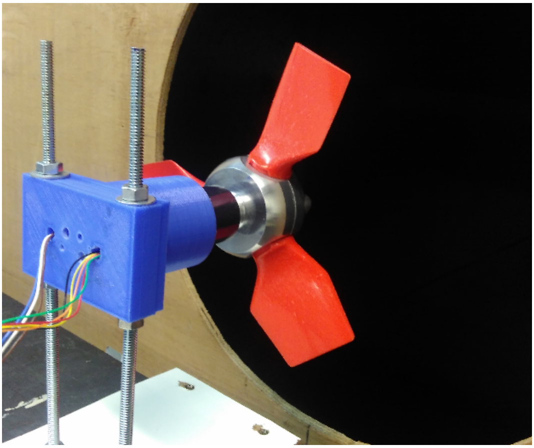

Figure 44 – Wind tunnel test.

From the mechanical power in the shaft of a turbine, given by Equation (2.8), the electrical power, P_E, can be obtained by considering all losses in the system. The result is expressed by Equation (4.1), where η is the combined efficiency of the generator and the diode bridge, that constitute most of the losses.

$$P_E = \eta \cdot \frac{1}{2}\rho A v^3 C_P \tag{4.1}$$

Then C_p can be obtained by manipulating the Equation (4.1):

$$C_p = \frac{2P_E}{\eta \rho A v^3} \tag{4.2}$$

With the data from Table 4 and Table 5, the value for the combined efficiency of the generator and the diode bridge is estimated as 85 %. This estimation considers that the losses are the same across all operation points, a fair approximation that simplifies the further calculation.

As discussed in Section 2.2, C_p curves for a rotor usually are a function of the blades' pitch angle and the tip-speed ratio. The designed rotor allows to manually change the pitch, then it is interesting to take measurements for more than one blade position to fit a more accurate model. A sample of the dataset results obtained in the wind tunnel tests are disposed in Table 10. The column C_p is computed by using the experimental results and Equation (4.2).

Table 10 – Wind tunnel results.

Wind Speed [m/s]	Pitch [deg]	ω [RPM]	P_E [W]	C_p
13	15	5700	14	0.390
17	15	7400	25	0.311
20	15	9000	38	0.290
23	15	10700	55	0.276
13	25	4900	10	0.278
17	25	6200	17	0.211
20	25	7400	25	0.191
23	25	8700	36	0.181

The resulting data obtained from the wind tunnel test does not match the model expressed by Equation (2.10) with parameters from Table 1, then it is not a proper model for the designed system. This happens because the designed wind turbine differs greatly from the small-sized wind turbines available in the literature with respect to the rotor size, its operation rotational speed and wind velocity. Therefore, a new model that matches the experimental results is needed to simulate the system properly.

Equation (2.12) was chosen to model the system for being a simple function that can properly describe a wind turbine rotor. The least squares best fit algorithm was used to fit the parameters. The resulting expression is given by Equation (4.3).

$$C_p = -0.0011(\lambda + 0.0007\beta^2 - 5.37)e^{1.36\lambda} \tag{4.3}$$

With the model that represents the rotor fitted, it is possible to plot the power coefficient, C_p, as a function of the tip-speed ratio, as shown in Figure 45. The values are computed for a pitch angle of 15°.

The theoretical optimum tip-speed ratio λ_{opt} that corresponds to the MPP can be obtained by finding the maxima of Equation (4.3). The maximum is found by equaling the first derivative to zero. The following expressions consider a pitch angle of 15°.

$$\frac{\partial C_p}{\partial \lambda} = \frac{\partial \left(-0.0011 \cdot (\lambda - 5.2125) \cdot e^{1.36\lambda}\right)}{\partial \lambda}$$

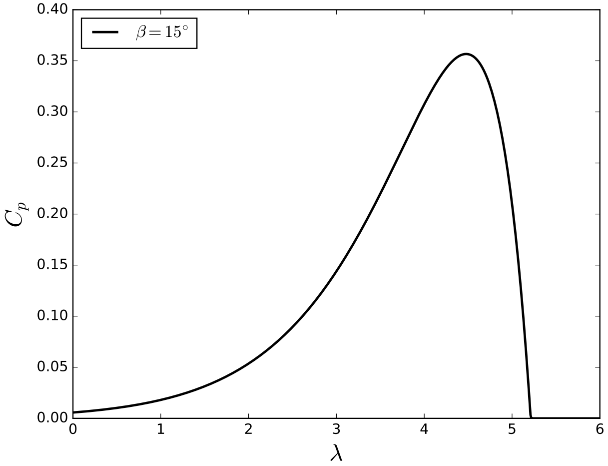

Figure 45 – Rotor C_p as a function of the tip-speed ratio.

$$\frac{\partial C_p}{\partial \lambda} = (0.0066979 - 0.001496\lambda) \cdot e^{1.36\lambda} \tag{4.4}$$

Then λ_{opt} is acquired by setting the first derivative to zero:

$$\frac{\partial C_p}{\partial \lambda} = 0$$

$$(0.0066979 - 0.001496\lambda) \cdot e^{1.36\lambda} = 0$$

$$\lambda_{opt} = 4.47721 \tag{4.5}$$

The computed value for λ_{opt} matches the Figure 45 plot. A second derivative test is not necessary because the results are visually compatible. The obtained result corresponds to the reference for the OTSR MPPT method.

The maximum power coefficient that the rotor can achieve with a pitch angle of 15° can be computed by replacing λ_{opt} value into Equation (4.3).

$$C_{p_{max}} = C_p(\lambda_{opt}) \tag{4.6}$$

$$C_{p_{max}} = 0.356675 \tag{4.7}$$

To determine the power that the rotor can convert from the available wind power Equation (2.8) altogether with the Equation (4.3) can be used. Figure 46 shows the model mechanical output power for different wind velocities.

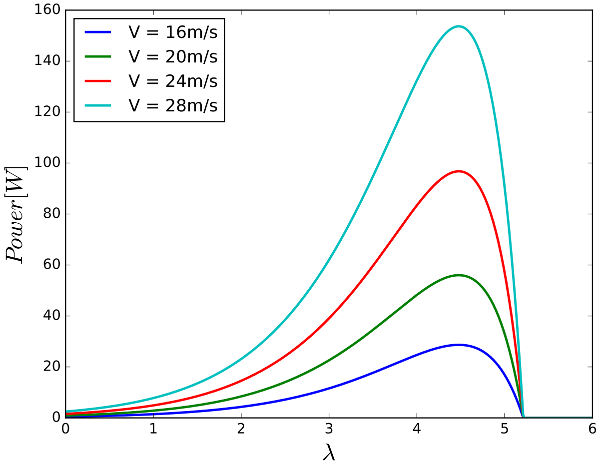

Figure 46 – Rotor output power as a function of the tip-speed ratio for different wind velocities.

Figure 47 shows the output power as a function of the rotor rotational speed for different wind velocities.

As discussed in Section 2.8, a cubic function can be fitted to express the MPP as a function of the rotational velocity. This is done by applying the least squares algorithm to fit the coefficient of Equation (2.44) with the model maximum values for each wind speed. The result is given by Equation (4.8). Figure 48 shows the cubic fitted function overlaying the power curves. This resulting equation allows to implement the PSF MPPT method.

$$P_{m_{opt}} = 0.000000075 \cdot \omega_m^3 \tag{4.8}$$

4.2 GENERATOR AND RECTIFIER

To model the generator and rectifier the circuit simulation software PSIM was chosen. It is a reliable and accurate software widely

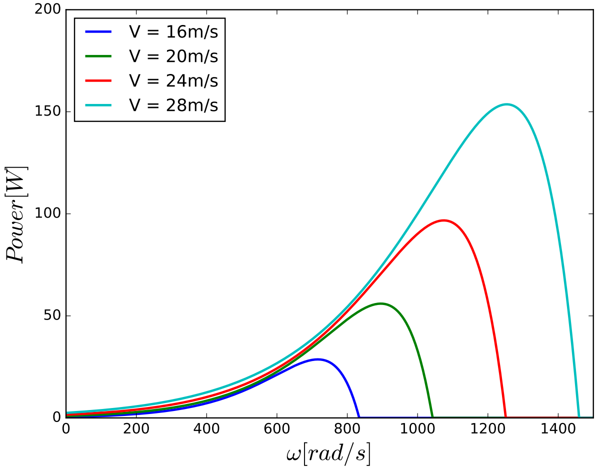

Figure 47 – Rotor model mechanical power of as a function of the rotational speed.

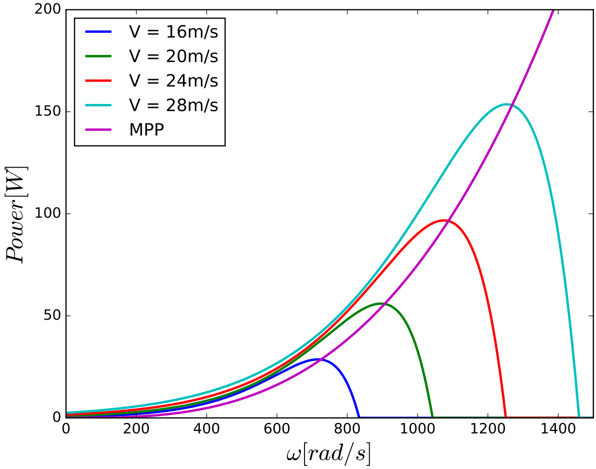

Figure 48 – Cubic MPP curve as a function of the rotational speed.

used for simulation of power electronics circuits. The BLDC and bridge rectifier models available in PSIM follow the same equations presented in Chapter 2. With the specifications from Table 4 and Table 5 it is possible to make realistic simulations that behave similarly to the real system.

4.3 BATTERY

A good battery model is of great importance in battery-powered system development, allowing to make realistic simulations. The aim of these models is to describe the characteristics of a battery and estimate its state-of-charge (SOC) and state-of-health (SOH). Among the three usual types of battery models, the experimental, electrochemical and based in electric circuit, the last is the preferred to represent electrical characteristics and make simulations.

(TREMBLAY; DESSAINT; DEKKICHE, 2007) proposes a battery model using a controlled voltage source with a constant resistance, represented in Figure 49. The controlled source reference E, that is the voltage with no losses caused by the internal resistance, is given by Equation (4.9).

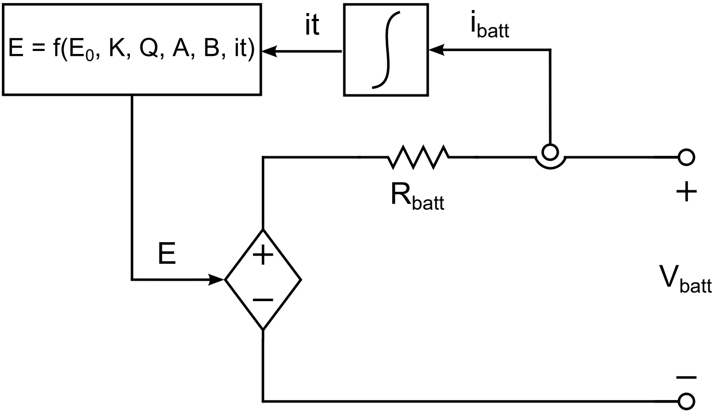

Figure 49 – Non linear battery model circuit.

$$E = E_0 - K\frac{Q}{Q - \int idt} + Ae^{-B\int idt} \tag{4.9}$$

Where:
E = no-load voltage [V];
E_0 = battery constant voltage [V];
K = polarization voltage [V];
Q = battery capacity [A h];
$\int idt$ = actual battery charge [A h];
A = exponential zone amplitude [V];
B = exponential zone time constant inverse $[\mathrm{A\,h}]^{-1}$.

And the output battery voltage is expressed by Equation (4.10).

$$V_{batt} = E - R_{batt} \cdot i_{batt} \tag{4.10}$$

Where:
V_{batt} = battery voltage [V];
R_{batt} = internal battery resistance [Ω];
i_{batt} = battery current [A].

By using the data from the battery cell datasheet, disposed in Table 5, and with some manual adjustments to fit the results with the experimental data from the manufacturer, the obtained parameters for the battery cell model are shown in Table 11.

Table 11 – Battery cell model parameters.

E_0 [V]	3.3
K [V]	0.05
Q [A h]	2.5
A [V]	0.44
B $[\mathrm{A\,h}]^{-1}$	10.0
R_{batt} [Ω]	0.006

Figure 50(a) shows the constant power discharge curves provided by the manufacturer available in (A123 SYSTEMS, 2012) and Figure 50(b) shows the simulation curves obtained using the parameters from Table 11.

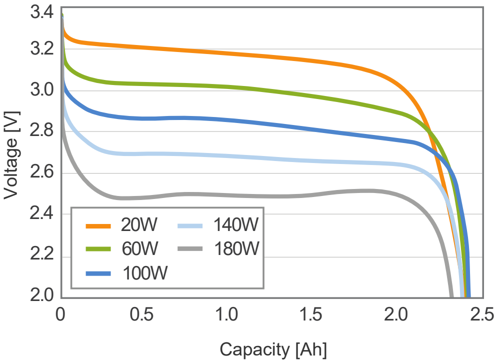

(a) Datasheet.

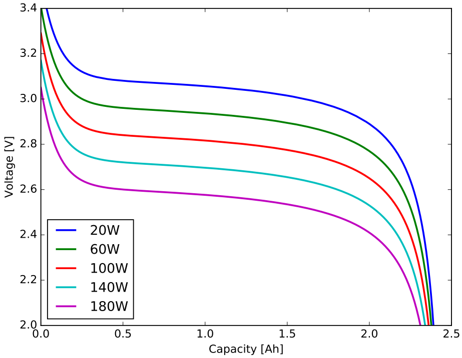

(b) Simulation.

Figure 50 – Battery cell constant power discharge characteristics.
Source: (A123 SYSTEMS, 2012).

5 SIMULATION RESULTS

In Chapter 3 the design of each wind turbine module was described and in Chapter 4 ways to model the system were discussed. Now, with a good comprehension of the entire system and the proper models designed, it is possible to evaluate the proposed strategies to achieve the MPPT.

The following results were obtained by conducting simulations with the designed model using the software PSIM. The simulation results are crucial to understand the behavior of the system and assess the feasibility of each proposed MPPT method before any experimental tests on field.

5.1 DC-DC CONVERTER

To confirm that the designed non inverting Buck-Boost fulfills the voltage and current requirements some simulations with the system in steady state were made. The maximum voltage ripple value can be obtained by manipulating Equation (3.19):

$$\Delta V_{max} = \frac{I_o D_{max}}{C \cdot f_s} \tag{5.1}$$

$$\Delta V_{max} = 0.178\,\mathrm{V} \tag{5.2}$$

Figure 51 shows the simulated output voltage. The maximum voltage ripple that resulted from this simulation was 0.176 V.

The maximum current ripple value is obtained by manipulating Equation (3.17):

$$\Delta I_{max} = V_o \cdot \frac{1 - Dmin}{L \cdot f_s} \tag{5.3}$$

$$\Delta I_{max} = 0.242\,\mathrm{A} \tag{5.4}$$

Figure 52 shows the simulated output current. The simulation resulted in a maximum current ripple of 0.239 A.

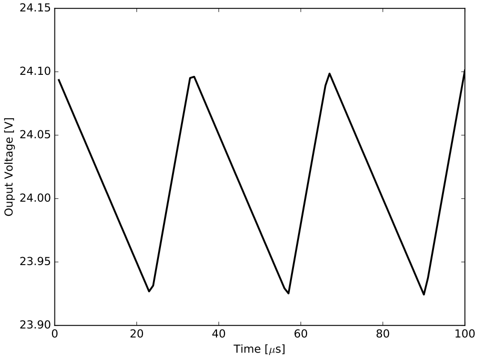

Figure 51 – Output voltage maximum ripple.

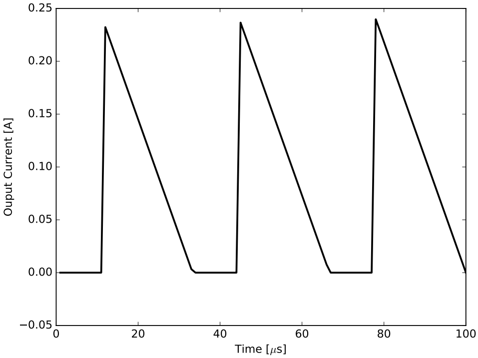

Figure 52 – Output current maximum ripple.

5.2 BATTERY

To evaluate the behavior of the battery using the CCCV charging method, the designed model can be used.

Figure 53 shows the battery charging with no load attached to it. While the constant current is applied to the battery the voltage across its terminals increase. When the battery reaches the fluctuation voltage, the current exponentially goes to zero. During the charging process the state of charge increases, reaching its operational value.

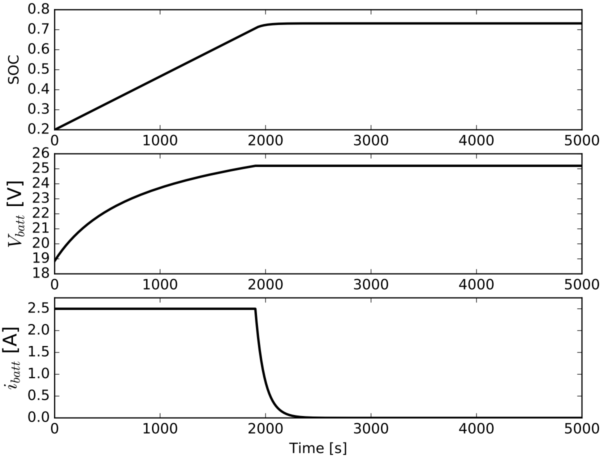

Figure 53 – Open circuit modeled battery CCCV charging method.

When a load of 30 W is attached to the battery terminals, the charging process becomes slower, as part of the input current goes to the load. After reaching the floating voltage, the input current exponentially drops to the current demanded by the load, avoiding the battery state of charge to decrease, as shown in Figure 54.

5.3 WIND TURBINE SYSTEM

With the models and simulation files for the rotor and the converter, it is possible to simulate the wind turbine system. A diagram with the system used for the following simulations is presented in Figure 55.

The rotor rotational speed can be manipulated by changing the rectified voltage V_{cc}. This is done with changes in the DC-DC converter duty cycle D. Figure 56 shows the result of a simulation where the DC-DC non-inverting buck-boost is operating in boost mode only. It is important to notice how the output power is also related to the rotational speed, making it possible to use the duty cycle to track the MPP. The displayed signals are filtered to suppress the ripple caused by the converter switches resulting in a cleaner plot. In this simulation the battery was modeled as a constant voltage source to avoid that the

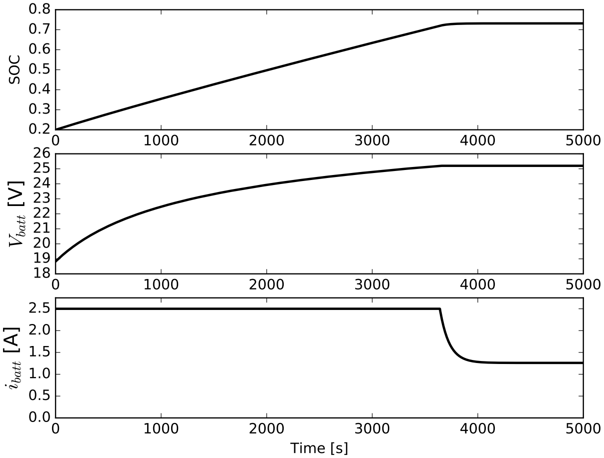

Figure 54 – Modeled battery CCCV charging method with 30W load.

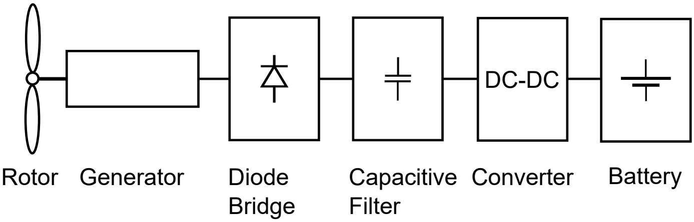

Figure 55 – Simulation system diagram.

output voltage changes with the state of charge.

With the simulation model it is also possible to trace the plots of the output power as a function of the rectified voltage V_{cc}, as expressed in Equation (2.47). Figure 57 shows the diagram of the simulated circuit used for this, that is similar to the diagram of Figure 55, but with a controlled voltage source replacing the battery and the DC-DC converter. This allows to analyze the system as the V_{cc} value changes while maintaining the wind speed constant. The results are displayed in Figure 58.

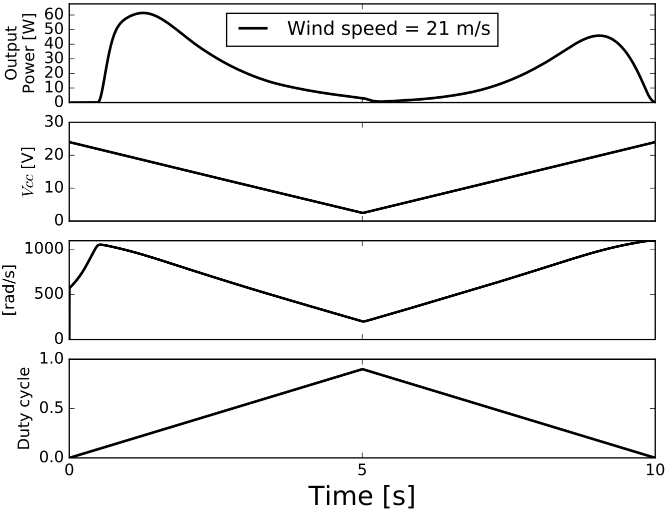

Figure 56 – Open loop simulation.

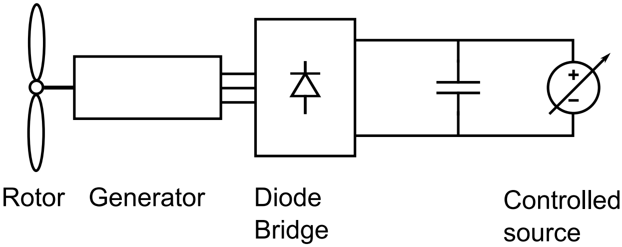

Figure 57 – Circuit simulation for obtaining the power output as a function of the rectified voltage.

Equation (5.5) is the resulting equation with the parameter K_V of Equation (2.47) fitted by using the least squares algorithm. The fitted cubic function over the power curves is shown in Figure 59.

$$P_{max} = 0.0067V_o^3 \tag{5.5}$$

With the circuit simulation represented in Figure 57 it is also

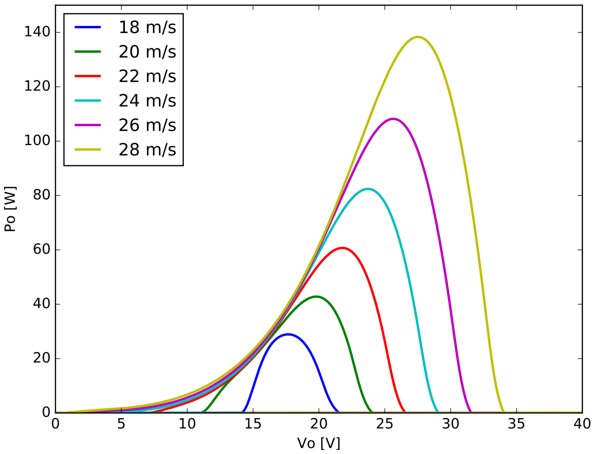

Figure 58 – Turbine model power curves versus rectified voltage.

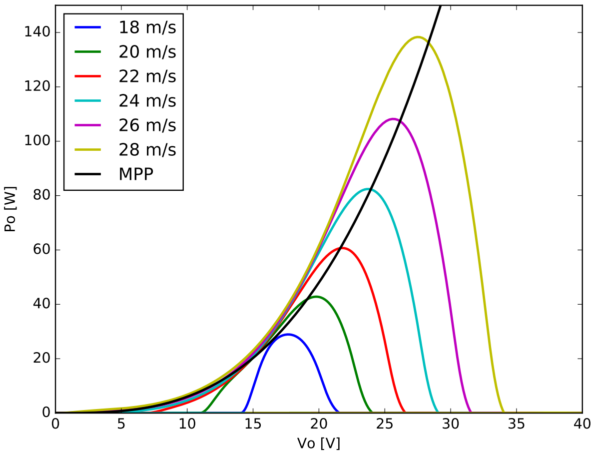

Figure 59 – Turbine model power curves with fitted cubic curve.

possible to evaluate the combined efficiency of the generator and the bridge rectifier. The efficiency, that is the ratio between the mechanical power driven by the rotor and the output electrical power, is shown in Figure 60. The efficiency is clearly dependent on the operation point. However, the efficiency results in steady state diverge little. Both results are around 82 %, close to the estimated value of 85 %.

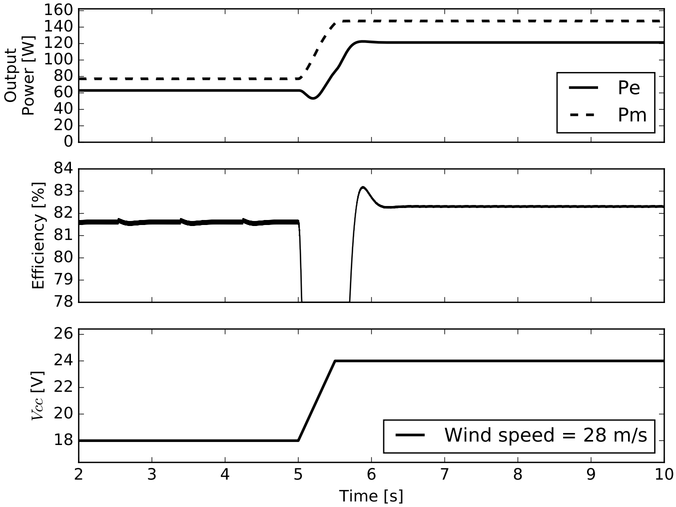

Figure 60 – Efficiency of the electrical components.

5.4 MPPT

5.4.1 PSF

The PSF method was simulated following the diagram in Figure 28, with the non inverting Buck-Boost converter performing as the DC-DC converter and a proportional-integral (PI) current controller. Figure 61 shows the simulation results. Pm and Pe are respectively the mechanical and electrical measured power. Pm_{max} represents the theoretical maximum power that the rotor can extract from the given wind. This is done by computing the maximum value of Equation (2.8) for the wind speed input, using Equation (4.3) as the rotor model. Pe_{max} is obtained with Equation (2.45), approximating the total electrical efficiency as 85 %. Ii is the rectified current, that is the system controlled variable. I_{ref} is the current reference. The results show that the current setpoint tracking was achieved by the PI controller. The electrical power curves show that the MPPT was achieved, with the electrical power converging to the theoretical maximum value. The mechanical power also converged to the theoretical MPP, confirming that the constant electrical efficiency assumption is near to the obtained with the PSIM simulation models for the generator and the diode bridge.

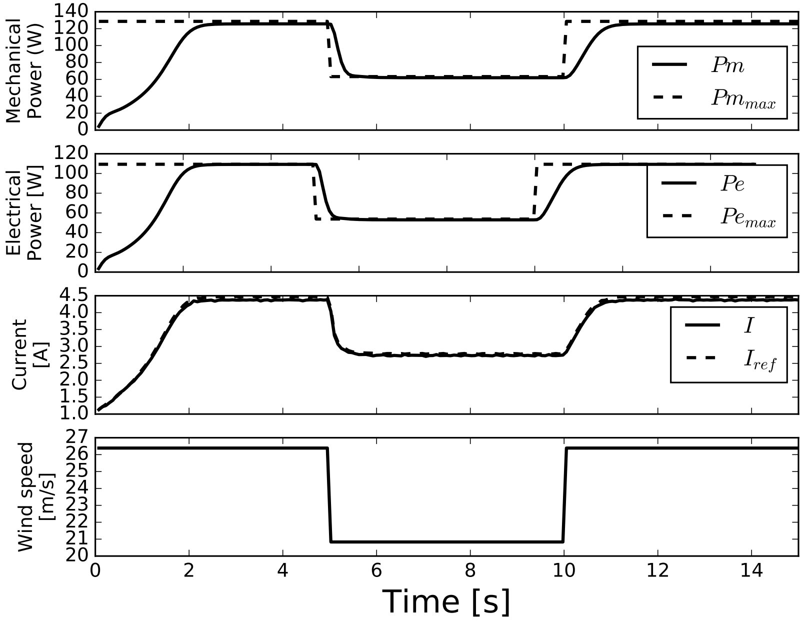

Figure 61 – PSF MPPT simulation with boost converter.

5.4.2 OTSR

To evaluate the OTSR method a PSIM circuit reproducing the diagram of Figure 26 was used. The results, demonstrated in Figure 62, show that the MPPT was nearly achieved, with a small difference that is caused by some approximation in the optimum tip-speed ratio. To make the system able to track the maximum power perfectly, the λ_{ref} must match precisely the turbine optimum value.

It is important to point out how this method suffers from abrupt variations in the wind velocity. It happens because λ is inversely proportional to the measured wind velocity, causing its value in the simulation to present peaks when the wind steps up or down. Although the wind is not expected to change as a step, it is important to evaluate the wind profile in the turbine operation to avoid unexpected behavior in the MPPT system.

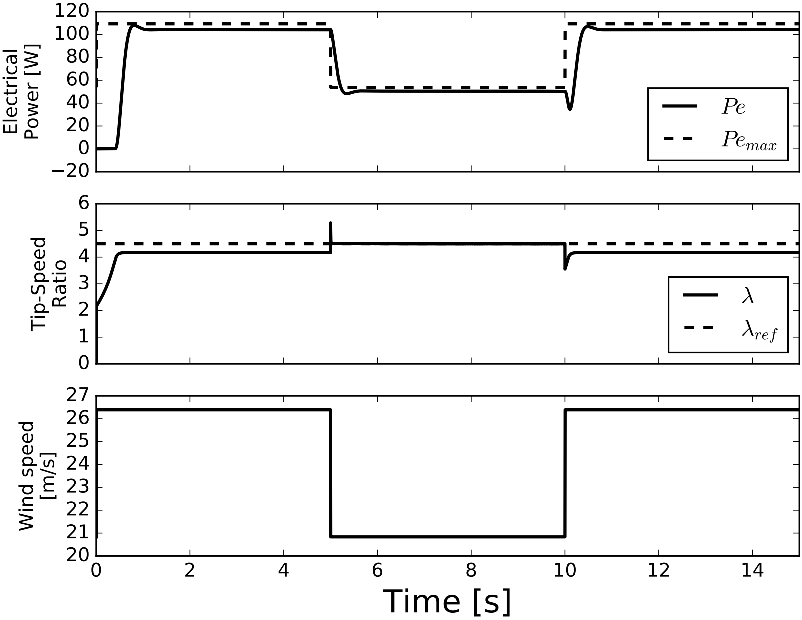

Figure 62 – OTSR MPPT simulation with boost converter.

6 EXPERIMENTAL RESULTS

This chapter will focus on the experimental tests that were conducted to verify the validity of the developed converter, wind turbine system and the proposed MPPT methods.

6.1 DC-DC CONVERTER

After the converter and driver PCBs manufacturing and the components soldering it is possible to test if the system achieved the desired design specifications. The first test consists in measuring the inductor current ripple with the system operating at the nominal current and maximum duty cycle, values that are disposed in Table 6. The results, obtained with a digital oscilloscope, are shown in Figures 63(a) and 63(b). The first figure shows the AC decoupled current signal. Removing the DC offset allows to show only the ripple signal. The latter figure shows the same signal along the duty cycle applied to the converter. The measured maximum ripple resulted in 206 mA, bellow the simulation result shown in Figure 52.

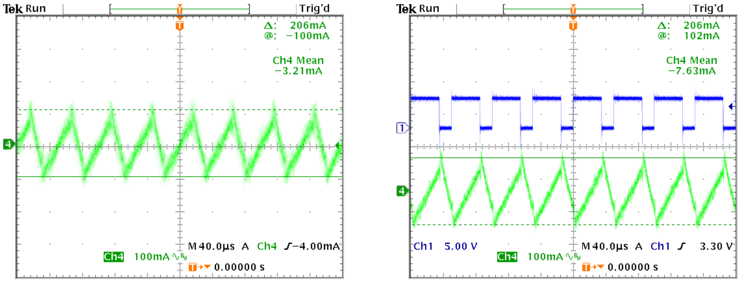

(a) Current ripple. (b) Current ripple and PWM signal.

Figure 63 – NIBB experimental current ripple.

Afterwards, the converter efficiency was measured with a 12 V source used as the input signal and a 25 Ω resistor as the output load. Figures 64(a) and 64(b) show respectively the input and output electrical measures (current and voltage) for a 50 % duty cycle. Figures 65(a) and 65(b) show the equivalent measurements for a 70 % duty cycle. The input power for the 50 % and the 70 % duty cycle are respectively

4.75 W and 20.64 W while the correspondent output power are 3.38 W and 15.90 W. With these results it is possible to compute the converter efficiency for both operation points: 71.1 % and 77.0 %.

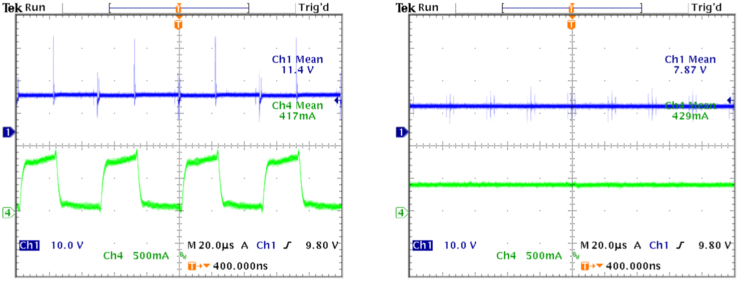

(a) Input.

(b) Output.

Figure 64 – (a) Input and (b) output voltages and currents with 50 % duty cycle.

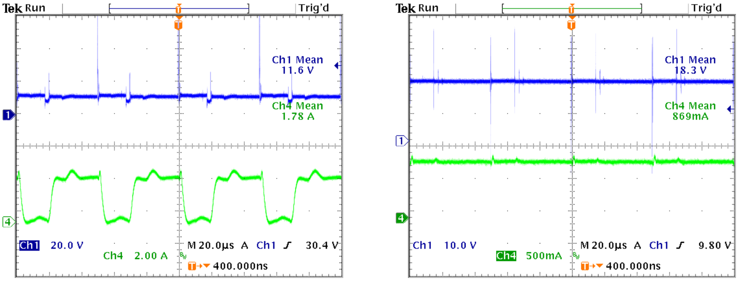

(a) Input.

(b) Output.

Figure 65 – (a) Input and (b) output voltages and currents with 70 % duty cycle.

Due to the higher capacitance capacitor used, the output voltage ripple is almost imperceptible, as shown in Figures 64(b) and 65(b).

The last converter test consists in measuring the static gain. This test used a 12 V input voltage source and a 50 Ω load, then the output voltage was measured for each duty cycle value. Figure 66 shows the experimental and theoretical expected results, obtained by using Equation (2.40).

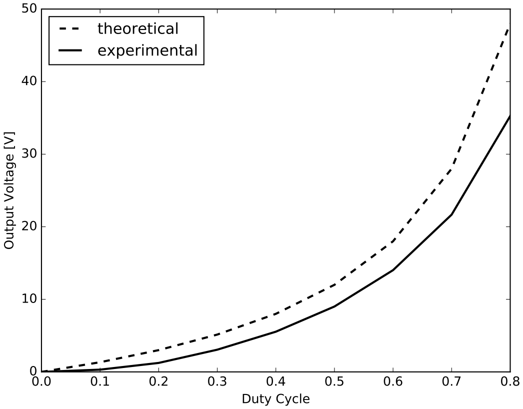

Figure 66 – NIBB theoretical and experimental static gain. 12 V input voltage and 50 Ω load.

6.2 OPEN LOOP

With the DC-DC converter tested and working as expected, it can be used to test how the output power can be manipulated by the converter duty cycle with a battery connected as the load. Knowing that the converter output voltage will be fixed by the battery, changing the duty cycle supposedly controls the input voltage V_{cc} and the generator rotational speed.

This test consists in using a 24 V battery as the load and taking the entire system to the wind tunnel. Then a ramp is applied through all the duty cycle range and the output power is measured. This is similar to the system described by Figure 57. Figure 67 shows the output power and rectified voltage V_{cc} results obtained for a wind speed of $18.5\,\mathrm{m\,s^{-1}}$.

The test was repeated for different wind speeds. Due to the noisy resulting data, the data was filtered and fitted to a Gaussian function to give a better understanding of the results, as represented in Figure 68. With the smoothed curves it is possible to compute the maximum output power. The results are disposed in Table 12.

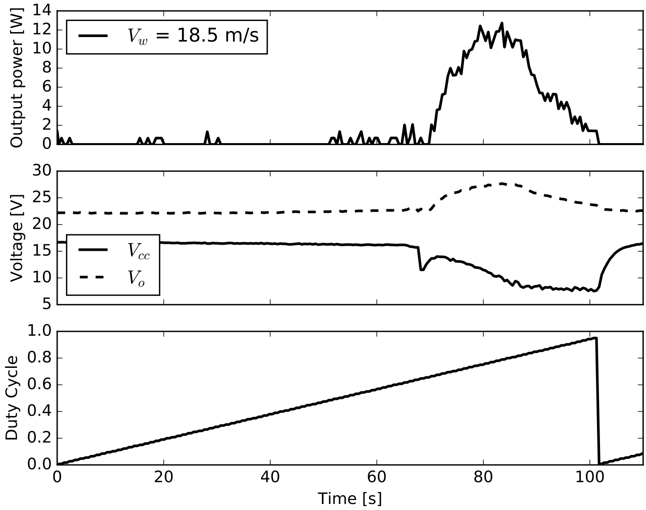

Figure 67 – Output power as a function of the NIBB duty cycle with $18.5\,\mathrm{m\,s^{-1}}$ wind speed.

Table 12 – Wind tunnel maximum output power with 24 V battery.

V_w $[\mathrm{m\,s^{-1}}]$	$P_{o_{max}}$ [W]
15.1	5.4
18.5	12.5
22.0	15.9
25.3	27.9

6.3 MPPT

Unfortunately testing the OTSR method was not possible because the wind tunnel output area is small, as shown in Figure 44, and does not have enough room for placing both the wind turbine and the anemometer.

The PSF method experimental test was also unsuccessful, because the hall sensor resolution was not sufficient to measure low rotational speeds. Since the speed decreases significantly as the output

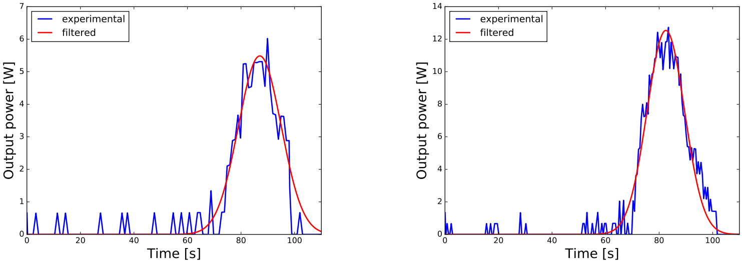

(a) $V_w = 15.1\,\mathrm{m\,s^{-1}}$.

(b) $V_w = 18.5\,\mathrm{m\,s^{-1}}$.

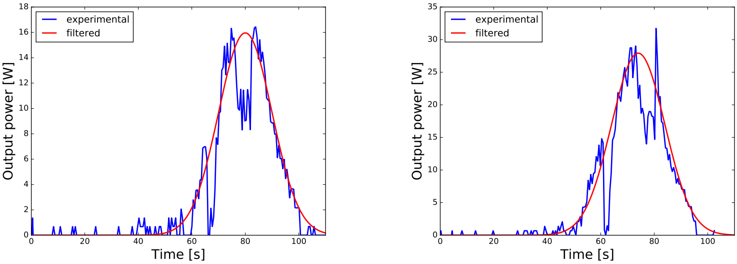

(c) $V_w = 22.0\,\mathrm{m\,s^{-1}}$.

(d) $V_w = 25.3\,\mathrm{m\,s^{-1}}$.

Figure 68 – Experimental and filtered output power as a function of the duty cycle for different wind speeds. 24V battery as output load.

power grows, the number of ticks from the sensor within the control loop frequency was not sufficient to compute the ω value. It is important to notice that any ω measurement error can lead to a great power tracking error as the MPP model is a function of the rotational speed to the power of 3. Using a higher resolution encoder should be enough to overcome this problem.

6.3.1 P&O

P&O proved to be most simple method to implement, for not depending on the system model and requiring to measure only the converter input current and voltage. The test consisted in applying a set of wind speed steps to verify if the MPPT method was able to track the maximum power. The resulting converter input and output power along with the duty cycle and the input wind speeds are shown in Figure 69.

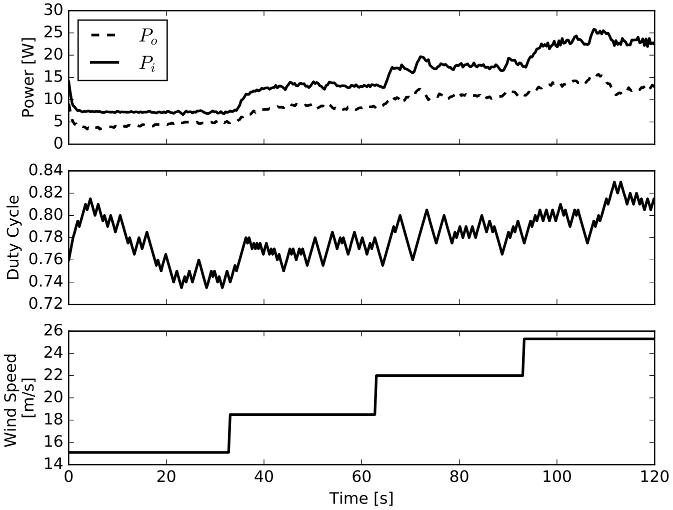

Figure 69 – P&O results.

The output power applied to the battery compared with the maximum possible values, disposed in Table 12, is shown in Figure 70.

Figure 70 shows the output power, P_o, compared with the maximum possible values $P_{o_{max}}$, disposed in Table 12. The output power values obtained from an open loop experiment, $P_{o_{open}}$, are also shown.

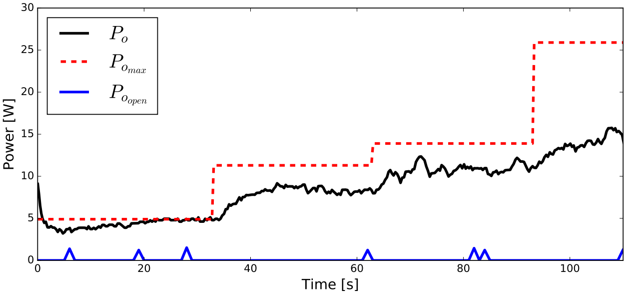

Figure 70 – P&O output power tracking.

The Arduino P&O developed code is attached in Appendix D.

7 CONCLUSION

This master thesis aimed at the development of a system able to provide energy constantly to an AWE pumping kite control unit during its flight operation. The proposed solution consisted in developing a micro wind turbine system that can be attached to the pumping kite control pod.

After an introductory chapter, where the problem was introduced in conjunction with an overview of the AWE design concept, describing more deeply the pumping kite configuration, the most important wind power system theoretical fundamentals for this project were discussed. Many wind turbine design techniques and components just apply to bigger turbines, then it is essential to revise the literature and filter what can be applied to such small scaled system. First the equations that express the available wind power were presented. Afterwards the possible designs for a wind turbine rotor and its models commonly used in the literature were discussed. The generator is another important element in the system. It was proposed to use a BLDC machine as the generator, being a high efficiency machine with relatively small cost and reduced weight and dimensions. The equations that describe how the BLDC works were also presented. With such generator, a rectifier is needed to convert the AC three-phase output into DC. To understand how a rectifier works, both single and three-phase topologies were presented. The DC-DC converter is the element responsible to manipulate the turbine power, allowing to implement a MPPT technique. Four topologies were described: the Buck, the Boost, the Buck-Boost and the non-inverting Buck-Boost converter. Afterwards a study about the most relevant battery technologies was shown. In the end of this chapter three MPPT methods were presented: OTSR, PSF and P&O.

After the manufacturing of all components, a proper modeling for the system allowed to obtain simulation results. The rotor model obtained from literature was not coherent with the results from the first wind tunnel tests, then a modeling method using the experimental results and the least square algorithm to fit a non linear function model was proposed.

Then a prototype was assembled and experimental tests performed. The designed NIBB converter ripple current and voltage results were within the expected. However the static gain did not match the theoretical results. It is hard to achieve a good efficiency when working with a low power converter, then some extra research can be applied to increase the 80% efficiency that the converter presented. A viable approach would be to replace the converter diodes and use Schottky diodes, that have a lower forward voltage drop when compared to the MUR820 device. Also, some newer FET technologies have better efficiency than the IRF640 used in the prototype, like the Infineon CoolMOS^{TM} devices, with Drain-Source resistances as low as $40\,\mathrm{m}\Omega$ (INFINEON, 2016), almost 4 times lower than the IRF640 resistance.

The developed wind turbine is not intended to work continuously in the MPP. Only the power needed to keep the battery charged must be generated, because the more power is produced the more drag is added to the pumping kite system. However MPPT methods are crucial to allow the system to extract the maximum power when it is necessary. Simulation or experimental tests were conducted to evaluate the three proposed MPPT methods:

- OTSR: The simulation results showed that abrupt variations in the wind speed causes overshoots in the output power, due to the reference being computed by dividing the tip-speed ratio by the rotational speed. Also, this method depends on two mechanical sensors: a rotational speed sensor and an anemometer. Testing this method in the wind tunnel was not possible as the wind tunnel output area was not sufficient to allocate both the rotor and the anemometer.

- PSF: The simulation results performed well for this method. However, it depends to much on the model and requires a good precision rotational speed sensor, because the optimal output power reference is a cubic function of the rotational speed. With the BLDC generator low resolution embedded Hall sensor, it was not possible to make accurate measures in low speeds, not allowing to succeed in the wind tunnel tests.

- P&O: This method was simple to implement for not depending on any system model. The power tracking was successful for small wind speeds in the wind tunnel tests. However, the MPPT was unable to track the maximum expected power in higher wind speeds. This happened because the converter static gain was not matching the theoretical values, then the duty cycle reached the saturation before the system achieved the maximum power point. Besides that, the perturbation size (voltage step) was a fixed value. This value should be proportional to the rotor rotational speed, because at lower speeds (consequently lower rectified voltages) a voltage change value is more significant to the output power then the same value change is applied while the system is at a higher speed.

Although the MPP was not achieved for higher wind speeds, when analyzing the results from Figure 70 it becomes clear that the open loop system is not able to generate power when connected to a 24 V battery. Therefore, even without a proper power tracking - that can be achieved by applying adjustments to improve its performance -, using the P&O method allowed the system to charge the battery.

With a single converter it is not possible to run the MPPT and CCCV charging method simultaneously, then an additional logic must be added to limit the output current and grant the correct battery charge, as proposed by (FARIAS et al., 2017). In critical moments the MPPT must be completely turned off to avoid disturbing the pumping kite operation, like during the land and takeoff and during the trajectory segments where the kite speed is low.

It is important to be noticed that during the wind tunnel power tracking tests, as shown in Figure 69 and Figure 70, the duty cycle applied to the converter was superior to 0.5 for every wind velocity input, that varied from $15.1\,\mathrm{m\,s^{-1}}$ to $25.3\,\mathrm{m\,s^{-1}}$. This is an indication that the NIBB worked just as a step-up converter. If further tests prove that this pattern is valid even with the higher desired wind speed of $30\,\mathrm{m\,s^{-1}}$, a Boost converter can be designed as a replacement for the proposed converter, with a higher efficiency for having less power components.

The P&O has proved to be the most simple MPPT method for requiring only the measurement of either the converter input or output power, that can be computed as the product of the measured voltage and current. Also, not requiring any model to track the maximum power is an advantage when the available models are not sufficient to describe the wind turbine system, because raising the data and fitting a proper model is a tiresome process that involves several tests in the wind tunnel, choosing the most appropriate non-linear function and using some algorithm to fit the data to the coefficients.

The wind tunnel tests using a resistive load connected directly to the rectifier output proved that the designed wind turbine is able to generate an output power superior to 60 W. However, with a 24 V battery connected to the NIBB converter output the maximum obtained power did not surpass 30 W for a wind speed of $25\,\mathrm{m\,s^{-1}}$. Using a wind tunnel that reaches 30 m s^{-1} will allow the wind turbine to produce more power, but to reach the desired 60 W a higher efficiency converter is needed.

7.1 FUTURE WORK

The suggestions for future works related to this thesis are:

- To develop a higher efficiency DC-DC converter. This can be done by replacing the NIBB converter topology for a Boost converter, that usually presents smaller losses for having a single switch. Replacing the diodes and transistors for more efficient devices along with the study and implementation of other switching methods for the NIBB converter can also increase the system efficiency.
- To perform tests in a wind tunnel that reaches the wind speed of 30 m s^{-1} to cover the entire desired range while evaluating the power tracking. Also a wind tunnel with a wider output area would allow to use an anemometer and the wind turbine simultaneously. With an anemometer the OTSR MPPT method could be implemented.
- To use a higher precision rotational speed sensor to allow the tests of the PSF MPPT method in a wind tunnel.
- To optimize the hardware to allow the P&O algorithm operation to track the maximum power for every wind speed. This consists in using less noisy current sensors and replacing the converter with a more efficient circuit. It is also necessary to make small adjustments to enable this method to perform better. Firstly, the applied perturbation step must be proportional to the turbine rotational speed, or even to the output power, avoiding the algorithm to get stuck when the noise magnitude is more expressive than the perturbation. Also the sample time is a value that can be better adjusted in order to achieve the tracking quicker, respecting the system settling time.
- To implement a complementary algorithm logic to enable the MPPT in conformity with the battery SOC and the pumping kite trajectory. Preferably this supervisory system must compute a power reference to limit the output power to avoid generating unnecessary energy.

- To manufacture the proposed new control pod design to test the system during the flight of a pumping kite system.
- To implement further circuitry to operate the battery safely, as a cell-balancing and a power path circuits.

BIBLIOGRAPHY

A123 SYSTEMS. *Nanophosphate High Power LithiumIon Cell ANR26650M1-B datasheet.* [S.l.], 2012.

AHRENS, U.; DIEHL, M.; SCHMEHL, R. **Airborne wind energy**. [S.l.]: Springer Science & Business Media, 2017.

ALLEGRO. **ACS712 Hall Effect-Based Linear Current Sensor IC Datasheet**. [S.l.], 2017.

AMERESCO SOLAR. **60W PHOTOVOLTAIC MODULE - 60J**. [S.l.], 2015.

ARGATOV, I.; RAUTAKORPI, P.; SILVENNOINEN, R. Estimation of the mechanical energy output of the kite wind generator. v. 34, p. 1525–1532, 06 2009.

ATMEL. **Atmel ATmega328P Datasheet**. [S.l.], 2011.

BARBI, I. **Modelagem de conversores CC-CC empregando modelo médio em espaço de estados**. [S.l.]: Author's edition, 2015.

BARBI, I.; FONT, C. H. I.; ALVES, R. L. Projeto físico de indutores e transformadores. **Internal document (INEP–2002)**, 2002.

BIANCHI, F. D.; MANTZ, R. J.; BATTISTA, H. D. **The wind and wind turbines**. [S.l.]: Springer, 2007.

DANEKAR, A. V. Analysis and design of high-frequency soft-switching dc-dc converter for wireless power charging applications. 2017.

De LELLIS, M. **Airborne wind energy with tethered wings: modeling, analysis and control**. Tese (Doutorado) — Federal University of Santa Catarina, Florianopolis, Brazil, 2016.

ELGENDY, M. A. Comparative investigation on hill climbing mppt algorithms at high perturbation rates. In: **2016 7th International Renewable Energy Congress (IREC)**. [S.l.: s.n.], 2016. p. 1–6.

FAGIANO, L. et al. Autonomous takeoff and flight of a tethered aircraft for airborne wind energy. **IEEE Transactions on Control Systems Technology**, v. 26, n. 1, p. 151–166, Jan 2018. ISSN 1063-6536.

FARIAS, G. de C. et al. A wind energy battery charging system with dynamic current limitation for output power limiting. In: **2017 IEEE 8th International Symposium on Power Electronics for Distributed Generation Systems (PEDG)**. [S.l.: s.n.], 2017. p. 1–7.

GRIGSBY, L. L. et al. **The electric power engineering handbook**. [S.l.]: CRC Press Boca Raton, 2001.

HALL, P. J.; BAIN, E. J. Energy-storage technologies and electricity generation. **Energy policy**, Elsevier, v. 36, n. 12, p. 4352–4355, 2008.

HEIER, S. **Grid integration of wind energy: onshore and offshore conversion systems**. [S.l.]: John Wiley & Sons, 2014.

HUA, A. C.-C.; SYUE, B. Z.-W. Charge and discharge characteristics of lead-acid battery and lifepo4 battery. In: IEEE. **Power Electronics Conference (IPEC), 2010 International**. [S.l.], 2010. p. 1478–1483.

IEA. Technology roadmap wind energy. OECD Publishing, 2013.

IEA. World energy outlook 2016. p. 684, 2016.

INFINEON. **Infineon CoolMOS IPB60R040C7 Datasheet**. [S.l.], 2016.

JAIN, P. **Wind energy engineering**. [S.l.]: McGraw-Hill,, 2011.

KIEBOOM, B. V. D. Design and noise study of a low-drag wind turbine for airborne power applications: A numerical and experimental assesment. 2017.

KUIK, G. A. V. The lanchester–betz–joukowsky limit. **Wind Energy**, Wiley Online Library, v. 10, n. 3, p. 289–291, 2007.

KUMAR, D.; CHATTERJEE, K. A review of conventional and advanced mppt algorithms for wind energy systems. **Renewable and sustainable energy reviews**, Elsevier, v. 55, p. 957–970, 2016.

LACZKO, A. A. et al. Modeling and simulation of a brushless dc permanent-magnet generator-based wind energy conversion system. In: IEEE. **Ecological Vehicles and Renewable Energies (EVER), 2015 Tenth International Conference on**. [S.l.], 2015. p. 1–7.

LINDEN, D. Handbook of batteries and fuel cells. **New York, McGraw-Hill Book Co., 1984, 1075 p. No individual items are abstracted in this volume.**, v. 1, 1984.

MAHDAVIAN, M. et al. Maximum power point tracking in wind energy conversion systems using tracking control system based on fuzzy controller. In: IEEE. **Electrical Engineering/Electronics, Computer, Telecommunications and Information Technology (ECTI-CON), 2014 11th International Conference on**. [S.l.], 2014. p. 1–5.

MAHMOUD, M. S.; XIA, Y. **Applied Control Systems Design**. [S.l.]: Springer Science & Business Media, 2012.

MANYONGE, A. W. et al. Mathematical modelling of wind turbine in a wind energy conversion system: Power coefficient analysis. **Applied Mathematical Sciences**, v. 6, n. 91, p. 4527–4536, 2012.

MILIVOJEVIC, N. et al. Electrical machines and power electronic drives for wind turbine applications. In: IEEE. **Industrial Electronics, 2008. IECON 2008. 34th Annual Conference of IEEE**. [S.l.], 2008. p. 2326–2331.

MOHOD, S. W.; AWARE, M. V. Micro wind power generator with battery energy storage for critical load. **IEEE systems journal**, IEEE, v. 6, n. 1, p. 118–125, 2012.

National Academy of Sciences. **Energy for Rural Development**: Renewable resources and alternative technologies for developing countries. Washington, D.C.: The National Academies Press, 1981.

PAULIG, X.; BUNGART, M.; SPECHT, B. Conceptual design of textile kites considering overall system performance. In: **Airborne wind energy**. [S.l.]: Springer, 2013. p. 547–562.

PEJOVIC, P. Three-phase diode bridge rectifier. **Three-Phase Diode Bridge Rectifier With Low Harmonics: Current Injection Methods**, Springer, p. 7–21, 2007.

PETKOVIĆ, D.; ĆOJBAŠIČ, Ž.; NIKOLIĆ, V. Adaptive neuro-fuzzy approach for wind turbine power coefficient estimation. **Renewable and Sustainable Energy Reviews**, Elsevier, v. 28, p. 191–195, 2013.

PILLOT, C. The rechargeable battery market and main trends 2014–2025. In: **31st International Battery Seminar & Exhibit**. [S.l.: s.n.], 2015.

PRAMOD, M. S. et al. Monitoring of highway wind power parameter and controlling highway light through iot. In: **2017 2nd IEEE International Conference on Recent Trends in Electronics, Information Communication Technology (RTEICT)**. [S.l.: s.n.], 2017. p. 1750–1753.

SILVA, R. S. d. et al. Aerofólios cabeados para geração de energia elétrica. 2014.

SIRA-RAMÍREZ, H.; SILVA-ORTIGOZA, R. **Control design techniques in power electronics devices**. [S.l.]: Springer Science & Business Media, 2006.

TIBOR, B.; FEDÁK, V.; DUROVSKY, F. Modeling and simulation of the bldc motor in matlab gui. In: **2011 IEEE International Symposium on Industrial Electronics**. [S.l.: s.n.], 2011. p. 1403–1407. ISSN 2163-5137.

TREMBLAY, O.; DESSAINT, L.-A.; DEKKICHE, A.-I. A generic battery model for the dynamic simulation of hybrid electric vehicles. In: IEEE. **Vehicle Power and Propulsion Conference, 2007. VPPC 2007. IEEE**. [S.l.], 2007. p. 284–289.

VISHAY. **Three Phase Bridge (Power Modules) 25A to 35A - Datasheet**. [S.l.], 2017.

VLUGT, R. van der; PESCHEL, J.; SCHMEHL, R. Design and experimental characterization of a pumping kite power system. In: **Airborne wind energy**. [S.l.]: Springer, 2013. p. 403–425.

WASYNCZUK, O.; MAN, D. T.; SULLIVAN, J. P. Dynamic behavior of a class of wind turbine generators during random wind fluctuations. **IEEE Power Engineering Review**, PER-1, n. 6, p. 47–48, June 1981. ISSN 0272-1724.

WOLBERG, J. **Data analysis using the method of least squares: extracting the most information from experiments**. [S.l.]: Springer Science and Business Media, 2006.

YEDAMALE, P. Brushless dc (bldc) motor fundamentals. **Microchip Technology Inc**, v. 20, p. 3–15, 2003.

ZHAO, J.; YU, Y. Brushless dc motor fundamentals application note. **MPS, Futur. Analog IC Technol**, p. 7–8, 2011.

APPENDIX A – Inductor Design

Finding an inductor that fulfills the requirements of a power converter is not always an easy task. Then it was decided that the inductor for this project would be manually manufactured. The following design steps follows the area-product method, as described by (DANEKAR, 2017). (BARBI; FONT; ALVES, 2002) also shows a detailed method to design an inductor properly.

The inductor design begins with the desired constraint values:

$$\boldsymbol{L} = 2.133\,\mathrm{mH} \tag{A.1}$$

$$\boldsymbol{fs} = 20\,\mathrm{kHz} \tag{A.2}$$

$$\boldsymbol{I_{L_{max}}} = 2.625\,\mathrm{A} \tag{A.3}$$

$$\boldsymbol{I_{L_{RMS}}} = 2.5\,\mathrm{A}, \tag{A.4}$$

where $\boldsymbol{L}$ is the desired inductance, $\boldsymbol{fs}$ is the switching frequency, $\boldsymbol{I_{L_{max}}}$ is the maximum inductor current given by Equation (3.29) and $\boldsymbol{I_{L_{RMS}}}$ is the inductor RMS current, that is the DC-DC converter nominal output current.

Then some constants are determined empirically:

$$\boldsymbol{B_{max}} = 0.25\,\mathrm{T} \tag{A.5}$$

$$\boldsymbol{J_{max}} = 450\,\frac{\mathrm{A}}{\mathrm{cm}^2}, \tag{A.6}$$

where $\boldsymbol{B_{max}}$ is the maximum flux density and $\boldsymbol{J_{max}}$ is the maximum current density.

The fill factor, $\boldsymbol{k_w}$, is the fraction of the core area that is actually filled by copper. This value is less than 1 because of the round shape of a wire and its insulation. A typical value is:

$$\boldsymbol{k_w} = 0.7 \tag{A.7}$$

The permeability constant $\boldsymbol{\mu_0}$ is given by:

$$\boldsymbol{\mu_0} = 4\pi \times 10^{-7}\,\mathrm{H\,m^{-1}} \tag{A.8}$$

The area-product is the product of core area, $\boldsymbol{A_c}$, and the window area, $\boldsymbol{A_w}$. The area-product can be obtained by the following expression:

$$\boldsymbol{A_c \cdot A_w} = \frac{\boldsymbol{L \cdot I_{L_{max}} \cdot I_{L_{RMS}}}}{\boldsymbol{B_{max} \cdot J_{max} \cdot k_w}} \tag{A.9}$$

$$\boldsymbol{A_c \cdot A_w} = 1.833\,\mathrm{cm}^4 \tag{A.10}$$

An appropriate core will be able to carry the flux without saturating and winding. The core model E-42/21/20 was chosen, with the following specifications:

$$\boldsymbol{A_c} = 2.4\,\mathrm{cm}^2 \tag{A.11}$$

$$\boldsymbol{A_w} = 1.57\,\mathrm{cm}^2 \tag{A.12}$$

Then, the number of turns, $\boldsymbol{n}$, is obtained by the following expression:

$$\boldsymbol{n} = \frac{\boldsymbol{L \cdot I_{L_{max}}}}{\boldsymbol{B_{max} \cdot A_c}} \tag{A.13}$$

$$\boldsymbol{n} = 97 \tag{A.14}$$

And the air gap length, $\boldsymbol{l_g}$ can be computed as follows:

$$\boldsymbol{l_g} = \frac{\boldsymbol{n^2 \cdot \mu_0 \cdot A_c}}{\boldsymbol{L}} \tag{A.15}$$

$$\boldsymbol{l_g} = 1.29\,\mathrm{mm} \tag{A.16}$$

The required wire cross section area is:

$$\boldsymbol{S_{wire}} = \frac{\boldsymbol{I_{L_{RMS}}}}{\boldsymbol{J_{max}}} \tag{A.17}$$

$$\boldsymbol{S_{wire}} = 5.5556 \times 10^{-3}\,\mathrm{cm}^2 \tag{A.18}$$

A 22 AWG wire was chosen for being the only one available. Its cross section area is:

$$\boldsymbol{S_{22AWG}} = 4.013 \times 10^{-3}\,\mathrm{cm}^2 \tag{A.19}$$

The chosen wire cross section area is smaller than the computed value, then 2 wires in parallel must be used to achieve the required cross section area. The number of parallel wires will be defined as:

$$\boldsymbol{N_{wp} = 2} \tag{A.20}$$

The minimum winding area, $\boldsymbol{A_{w_{min}}}$, is the area the wire will occupy if the fill factor is achieved:

$$\boldsymbol{A_{w_{min}}} = \frac{\boldsymbol{n \cdot S_{22AWG} N_{wp}}}{\boldsymbol{k_w}} \tag{A.21}$$

$$\boldsymbol{A_{w_{min}}} = 4.013 \times 10^{-3}\,\mathrm{cm}^2 \tag{A.22}$$

Considering that the inductor will be manually manufactured, the design must let a good margin to allow some gaps that can be present between the wire turns. A good practice is that the execution factor, $\boldsymbol{\eta_{exec}}$, must be less than 0.7. $\boldsymbol{\eta_{exec}}$ is defined as the ratio between the minimum area that the wire will occupy and the available winding area:

$$\boldsymbol{\eta_{exec}} = \frac{\boldsymbol{A_{w_{min}}}}{\boldsymbol{A_w}} \tag{A.23}$$

$$\boldsymbol{\eta_{exec}} = 0.686 \tag{A.24}$$

APPENDIX B – Data Acquisition Board

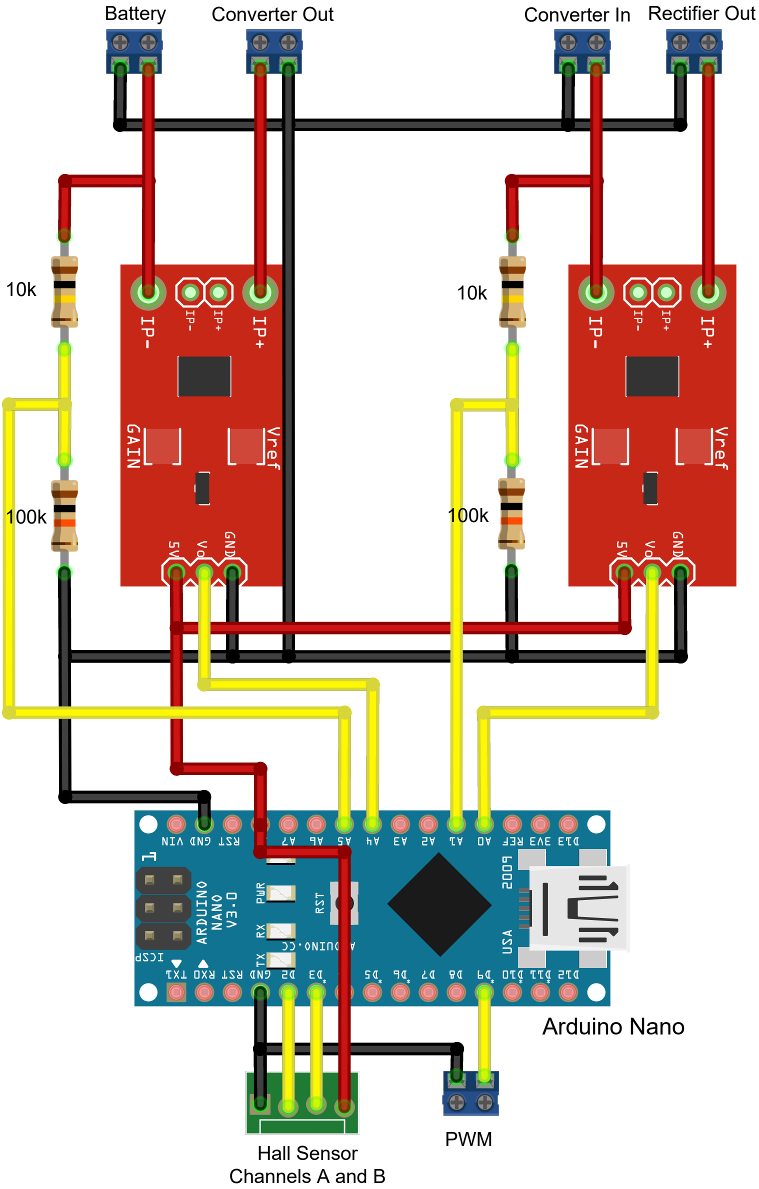

Figure 71 – Data acquisition board schematic.

APPENDIX C – Least Squares Method

Least squares is an analytical method used to extract information from a set of data, by adjusting the coefficients of a model function to fit the data set. The algorithm consists in finding parameters that are normally distributed around the coefficients of the real model with the least standard deviation possible. This appendix reproduces and adapts the work from (WOLBERG, 2006).

Least squares can be divided into two classes of problems, the linear least squares and nonlinear least squares. Every linear least squares problem can be represented by a function $\boldsymbol{y}$ of a vector $\boldsymbol{X}$ with $\boldsymbol{m}$ terms where all $\boldsymbol{p}$ unknown parameters are related only to the independent variables, i.e., the $\boldsymbol{m}$ terms of $\boldsymbol{X}$. Equation (C.1) represents this linear function.

$$\boldsymbol{y = f(X) = \sum_{k=1}^{p} a_k g_k(X)}$$

$$\boldsymbol{y = \sum_{k=1}^{p} a_k g_k(x_1, x_2 .... x_m)} \tag{C.1}$$

In cases where Equation (C.1) is applicable the problem can be solved directly by the least square method. However, when a function is not compatible with the linear form, an initial estimate is required and then the solution is achieved by recursive iterations until some convergence criterion is fulfilled.

C.1 LINEAR LEAST SQUARES

The fit of a model to a data point is measured by its residual, $\boldsymbol{R_i}$, that is the difference between the observed input, $\boldsymbol{y}$, and computed values of $\boldsymbol{\hat{y}}$ for the $\boldsymbol{i^{th}}$ data point.

$$\boldsymbol{R_i = y_i - \hat{y}_i} \tag{C.2}$$

$$\boldsymbol{R_i = y_i - f(X_i)} \tag{C.3}$$

The least squares solution is obtained by minimizing the sum of squared residuals, called objective function, $\boldsymbol{S}$, given by Equation (C.5). $\boldsymbol{X}$ is the the independent variables that can be scalar if there is only one independent variable or a vector if there is more than one independent variable. The function $\boldsymbol{f}$ is an equation that represents the relation between $\boldsymbol{X}$ and $\boldsymbol{\hat{y}}$. The variable $\boldsymbol{w_i}$ is the weight associated to the

i^{th} data point, used only when the constant variance assumption is not used ia a variation of the method called weighted least squares. Usually the data is supposed to be of equal quality, with constant variance, then the all the weights are defined as 1.

$$S = \sum_{i=1}^{n} w_i R_i^2 \tag{C.4}$$

$$S = \sum_{i=1}^{n} w_i \left(y_i - f(X)\right)^2 \tag{C.5}$$

To find the values of $a_k^\prime s$ that minimizes the function S it is necessary to set the p partial derivatives of S with respect to a_k to zero, as represented in Equation (C.6).

$$\frac{\partial S}{\partial a_k} = 0 \qquad k = 1, 2....p \tag{C.6}$$

Using Equation (C.5) with Equation (C.6) results in:

$$-2\sum_{i=1}^{n} w_i \left(y_i - f(X)\right) \frac{\partial f(X_i)}{\partial a_k} = 0 \qquad k = 1, 2....p$$

$$\sum_{i=1}^{n} w_i f(X_i) \frac{\partial f(X_i)}{\partial a_k} = \sum_{i=1}^{n} w_i y_i \frac{\partial f(X_i)}{\partial a_k} \qquad k = 1, 2....p \tag{C.7}$$

When the expression is linear, respecting Equation (C.1), the derivatives of f can be obtained easily:

$$\frac{\partial f(X)}{\partial a_k} = g_k(X) \qquad k = 1, 2....p \tag{C.8}$$

Then substituting Equation (C.8) into Equation (C.1) and manipulating leads to the following result:

$$\sum_{j=1}^{p} a_j \sum_{i=1}^{n} w_i g_j(X_i) g_k(X_i) = \sum_{i=1}^{n} w_i y_i g_k(X_i) \qquad k = 1, 2....p \tag{C.9}$$

The equation can be written using the following matrix notation, where C is a matrix with p rows and p lines, A and V are vector of length p:

$$\boldsymbol{CA = V} \tag{C.10}$$

And the terms $\boldsymbol{C_{jk}}$ and $\boldsymbol{V_k}$ are computed by the following expressions:

$$\boldsymbol{C_{jk} = \sum_{i=1}^{n} w_i g_j g_k} \tag{C.11}$$

$$\boldsymbol{V_k = \sum_{i=1}^{n} w_i y_i g_k} \tag{C.12}$$

A linear problem can be solved by computing the $\boldsymbol{a_k}$ terms of the vector A, that represent the unknown parameters of the system.

$$\boldsymbol{A = C^{-1} V} \tag{C.13}$$

C.2 NONLINEAR LEAST SQUARES

In order to solve problems where the function $\boldsymbol{f}$ is nonlinear a iterative approach is used. Initially a vector $\boldsymbol{a_k^0}$ with initial guesses for the unknown parameters must be chosen, then the estimated vector is updated by the algorithm:

$$\boldsymbol{a_k^{p+1} = a_k^p + \Delta a_k} \tag{C.14}$$

Where $\boldsymbol{\Delta a_k}$ is called the shift vector.

Nonlinear problems are more difficult to fit than linear because the solution cannot be obtained by using only matrix manipulation and linear algebra. The solution then is to use some method to linearize the model. Usually this is done by a approximation to a first order Taylor expansion about $\boldsymbol{a_k}$.

$$\boldsymbol{f(x_i) = f^j(x_i) + \sum_j \frac{\partial f(x_i)}{\partial a_k} \left(a_k - a_k^j\right)}$$

$$\boldsymbol{f(x_i) = f^j(x_i) + \sum_j J_{ik} \Delta a_k} \tag{C.15}$$

Where $\boldsymbol{J}$ is a Jacobian matrix, a matrix formed by all firs-order partial derivatives of a vector valued function.

The residual, $\boldsymbol{R_i}$, can be expressed as the difference of the observed value, $\boldsymbol{y}$ and the value computed by the Jacobian approximation in Equation (C.15):

$$\boldsymbol{R_i = y_i - f^j(x_i) - \sum_{k=1}^{m} J_{ik}\Delta a_k}$$

$$\boldsymbol{R_i = \Delta y_i - \sum_{k=1}^{m} J_{ik}\Delta a_k} \tag{C.16}$$

Then to obtain the least squares solution it is needed to minimize the residuals by solving the Jacobian for $\boldsymbol{\Delta a_k}$ and seting the gradient to zero:

$$\boldsymbol{-2\sum_{i=1}^{n} J_{ik}\left(\Delta y_i - \sum_{j=1}^{m} J_{ik}\Delta a_j\right) = 0} \tag{C.17}$$

That can be rearranged as a set of m simultaneous linear equations:

$$\boldsymbol{\sum_{i=1}^{n}\sum_{k=1}^{m} J_{ij}J_{ik}\Delta a_k = \sum_{i=1}^{n} J_{ij}\Delta y_i \qquad (j = 1, ..., m)} \tag{C.18}$$

And the equivalent matrix notation is given by:

$$\boldsymbol{(J_T J)\,\Delta a = J_T \Delta y} \tag{C.19}$$

C.3 ERROR DISTRIBUTIONS

To fit data with random variations, it is important to understand the error distribution and make some presumptions. Usually two assumptions are made. The first one is that the error is not present in the predictor data, but only in the response data. The second is that the errors are random, following a Gaussian distribution with zero mean and the variance constant. For most quantitative experiments both assumptions are true or at least a reasonable approximation. Equation (C.20) is a representation often used to express the former assumption.

$$\boldsymbol{error \approx N(0, \sigma^2)} \tag{C.20}$$

If the errors are completely random, the mean shall be zero.

Otherwise, if this value is different than zero the system may have systematic errors. The variance is related with the distribution of the errors. If the variance is constant, the distribution of the errors is also constant.

It is important to notice that the least-squares algorithm does not assume that the error is normally distributed, but this assumption is important because in normal distribution extreme random errors are uncommon, and least-squares has a poorer performance if data contain many random errors with extreme values. However, statistical results such as confidence and prediction bounds do require normally distributed errors for their validity.

APPENDIX D – Arduino P&O Source Code

```
#include <PWM.h>

#define pin_i1 A0
#define pin_v1 A1
#define pin_i2 A2
#define pin_v2 A3
#define pin_i3 A4
#define pin_v3 A5
#define pin_rpm 2
#define OUTPUT_PIN 9

//current sensor ACS720 5A constants
#define mVperAmp 160
#define ACSoffset 2495

//maximum duty cycle, range from 0 to 400
#define OUT_MIN 1
#define OUT_MAX 390

double p, io, icc, output = 0.0;
double vo, vcc, delP, delv, p_prev, v_prev = 0.0;

//variables for computing rotational speed
double omega = 0.0;
unsigned long rpm, half_rev = 0;
unsigned long timeold = millis();
int i = 0;
int out = 200; //initializing duty cycle as 0.5

void rpm(){//triggered by hall sensor external interrupt
    half_revolutions++;
    if (half_revolutions >= 20) {
        //Update RPM every 20 counts
        //increase this for better resolution
        rpm = 30*1000/(millis()-timeold)*half_rev;
        omega = rpm/9.5492965964; //RPM to rad/s
        timeold = millis();
        half_revolutions = 0;
    }
}

void setup(){
    InitTimersSafe();
    //sets switching frequency as 30kHz
    bool success = SetPinFrequencySafe(OUTPUT_PIN, 30000);
    attachInterrupt(digitalPinToInterrupt(pin_rpm),rpm,FALL);
    pinMode(pin_rpm, INPUT_PULLUP); //hall sensor pullup
    Serial.begin(115200);
    char a = 'b';
    while (a != 'a')
        a = Serial.read();//wait for serial command to start
```

```
}

void plot(){ //send data to serial
    Serial.println(vcc);
    Serial.println(icc);
    Serial.println(vo);
    Serial.println(io);
    Serial.println(delP);
    Serial.println(p_prev);
    Serial.println(rpm);
    Serial.println(out);
}

double measure_current(int pin){
    int MeasurementsToAverage = 20;
    int RawValue, temp = 0;
    double Voltage = 0;
    for(int i = 0; i < MeasurementsToAverage; ++i)
        temp += analogRead(pin);
    RawValue = temp/MeasurementsToAverage;
    Voltage = (RawValue / 1024.0) * 5000; //gets you mV
    double current = ((Voltage - ACSoffset) / mVperAmp);
    if (current < 0.0)//to avoid negative values
        current = 0.0;
    return current;
}

double measure_voltage(int pin){
    int MeasurementsToAverage = 20;
    int RawValue, temp = 0;
    double Voltage = 0;
    for(int i = 0; i < MeasurementsToAverage; ++i)
        temp += analogRead(pin);
    RawValue = temp/MeasurementsToAverage;
    return RawValue*5.0*10.35/1023.0;
}

int saturation(int value){//limit the PWM to the 0-400 range
    if (value == 255) //255 PWM sometimes causes trouble
        return (254);
    else if (value > OUT_MAX)
        return (OUT_MAX);
    else if (value < OUT_MIN)
        return (OUT_MIN);
    else
        return value;
}

void loop() {
    //measure voltages and currents
    vcc = measure_voltage(pin_v1)
    icc = measure_current(pin_i1);
```

```
    vo = measure_voltage(pin_v3)
    io = measure_current(pin_i3);
    //compute power
    p = vcc*icc;
    //compute delta P and V
    delP = p - p_prev;
    delv = vo - v_prev;

    if (delP < 0){
        if (delv <= 0)
            out+=2;
        else
            out-=2;
    }
    else {
        if (delv < 0)
            out-=2;
        else
            out+=2;
    }
    //change PWM value
    out = saturation(out);
    analogWrite(OUTPUT_PIN, out);

    //update previous values
    p_prev=p;
    v_prev=vo;

    //wait for the next iteration
    int delay_value = 200;
    delay(delay_value);

    //plot
    i++;
    if ((delay_value * i) >= 200){//to avoid flooding serial
        i = 0;
        plot();
    }
}
```

The PWM library is available at `https://code.google.com/archive/p/arduino-pwm-frequency-library/downloads`.